In situ characterization for boosting electrocatalytic carbon dioxide reduction

*Xueying Cao, Dongxing Tan, Bari Wulan, K.S. Hui, K.N. Hui, Jintao Zhang**

X. Cao, Dr. D. Tan, B. Wulan, Prof. J. Zhang
Key Laboratory for Colloid and Interface Chemistry, Ministry of Education, School of Chemistry and Chemical Engineering, Shandong University, Jinan 250100, PR China.
E-mail: jtzhang@sdu.edu.cn

Prof. K.S. Hui
School of Engineering, Faculty of Science, University of East Anglia, Norwich, NR4 7TJ, United Kingdom.

Prof. K.N. Hui
Joint Key Laboratory of the Ministry of Education, Institute of Applied Physics and Materials Engineering, University of Macau, Avenida da Universidade, Taipa, Macau SAR 999078, China.

Keywords: carbon dioxide reduction; *in situ*; reaction mechanism; electrocatalysis

The electrocatalytic reduction of carbon dioxide into organic fuels and feedstocks is a fascinating method to implement the sustainable carbon cycle. Thus, a rational design of advanced electrocatalysts and a deep understanding of reaction mechanisms are crucial for the complex reactions of carbon dioxide reduction with multiple electron transfer. *In situ* and operando techniques with real-time monitoring are important to obtain deep insight into the electrocatalytic reaction to reveal the dynamic evolution of electrocatalysts' structure and composition under experimental conditions. In this paper, the reaction pathways for the CO_2 reduction reaction (CO_2RR) in the generation of various products (e.g., C_1 and C_2) via the proposed mechanisms are introduced. Moreover, recent advances in the development and applications of *in situ* and operando characterization techniques, from the basic working principles and *in situ* cell structure to detailed applications, are discussed. Suggestions and future directions of *in situ*/operando analysis are also addressed.

1. Introduction

The massive accumulation of carbon dioxide with the rapid development of the industrial revolution driven by fossil fuels has substantially increased from about 280 ppm in the early 1800s to 415 ppm in 2019 and resulted in global warming and climate change because of the greenhouse gas effect.[1] Natural resources are rapidly depleting; thus, sustainable energies and technologies are urgently needed to restrain CO_2 emissions and develop efficient CO_2 utilization systems.[2] Carbon dioxide reduction reaction (CO_2RR) is a clean and efficient solution to address energy and environmental issues in one process.

CO_2 is a highly stable molecule with a high dissociation energy of about 750 kJ mol^{-1} because of the binding of sp-hybridized carbon atom with oxygen atoms via σ-bonds.[3] The reduction process of CO_2 with the highest chemical state (+4) of carbon atom is a complicated process with diverse products (i.e., C_1, C_2, and C_3). The formation of stable CO_2 radical anion ($*CO_2^-$) on the catalyst surface via the back donation of electrons from the highest occupied d orbital of a catalyst to the lowest unoccupied antibonding (π*) orbital of $*CO_2^-$ is a rate-determining step.[4] Various intermediates and products are then formed by the step-wise transfer of protons (H^+) and/or electrons (e^-) to active radicals.[4, 5] The possible reaction pathways with 2–14 e^- transfer for CO_2RR to form C_1 and C_2 products are summarized in **Figure 1a**. Specifically, for two-e^- transfer, *COOH is the more likely intermediate for CO formation, and *OCHO is the more likely intermediate for generating a formate product. Other C_1 products are converted from *CHO or *COH species with *CO as the intermediate. In comparison, C_2 pathways include *CO dimerization to form $*C_2O_2$ intermediate for the C–C bond step.[5, 6]

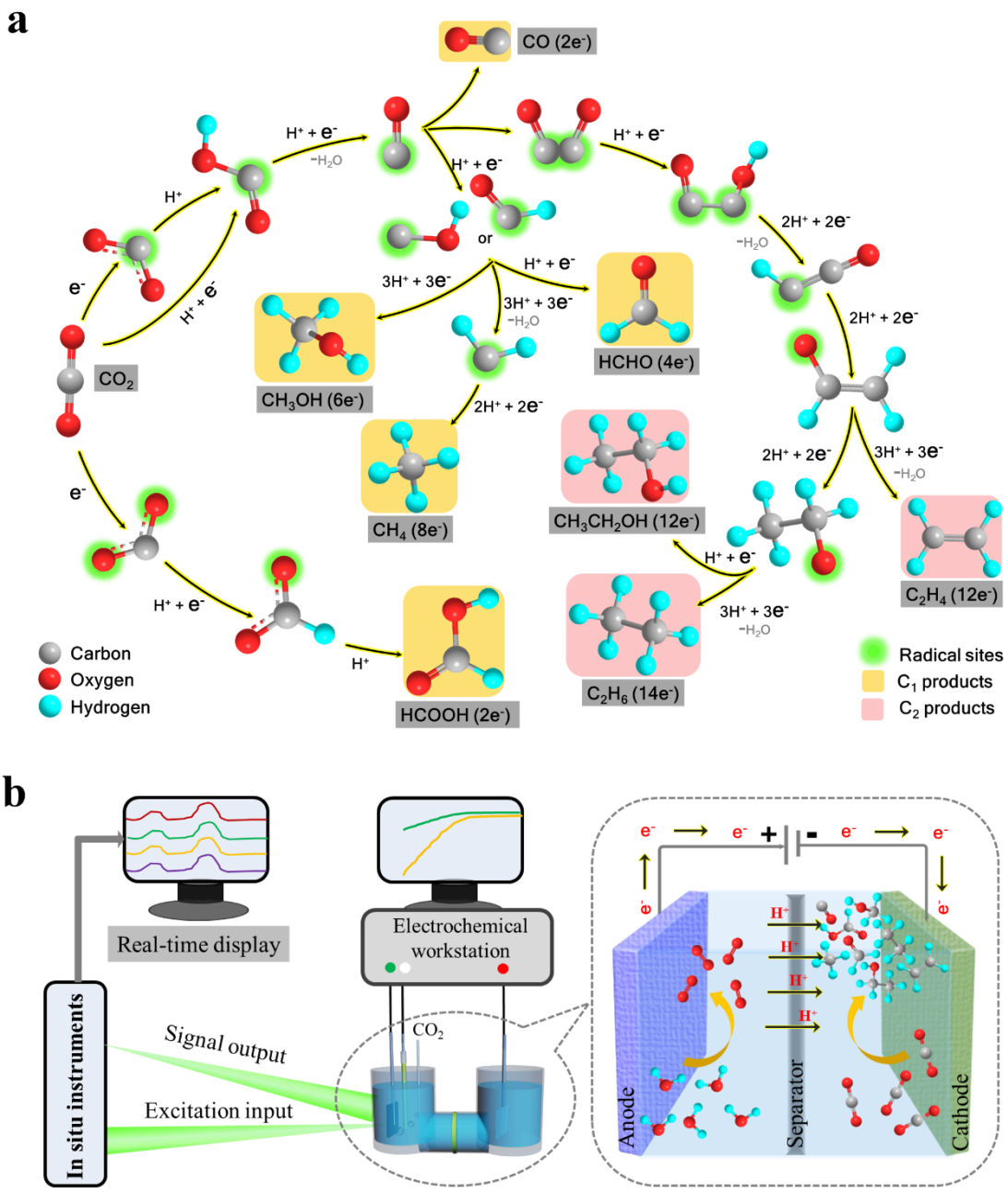

Figure 1. a) Sketch of possible reaction pathways for CO_2RR toward various C_1 and C_2 products. The curved arrows show the transfer pathways of proton, electron, and concerted proton–electron. b) Schematic of the basic configuration of *in situ* instruments. The right half is the schematic representation of electrochemical cells for CO_2RR.

Numerous efforts have been made in the past few years to ameliorate the reaction conditions to overcome the sluggish kinetics process of CO_2 reduction and the competitive hydrogen evolution reaction (**Table 1**). Many electrocatalysts can produce C_1 and C_2 products. However, current performances are far behind the technical demands for future applications,

and a valid solution requires a more targeted design of electrocatalysts through a deep understanding of active sites, intermediates, and reaction steps during CO_2RR.[7] Understanding the reaction mechanism of CO_2RR may lead to fundamental insights into the selectivity, activity, and stability of an electrocatalyst. A number of *ex situ* technologies, such as X-ray or vibrational analytical techniques, have been applied in the CO_2RR system, but the information collected through these techniques is restricted or limited because of inevitable changes during transfer and storage procedures.[8] Therefore, advanced *in situ*/operando characterization techniques are important to understand CO_2RR under real-time operating conditions. A schematic of the basic configuration of *in situ* instruments is shown in Figure 1b. The intelligent combination of an electrochemical system with characterization techniques is crucial to guarantee effective excitation input and signal output along with real-time information display during the CO_2RR process. Thus, minute details, such as the physical and chemical properties of materials, can be captured by advanced characterization techniques to reveal active sites and intermediates.

Table 1. Reduction potentials (vs. RHE) of related half-reactions in CO_2RR

Half-reaction	E (V vs. RHE)
$2H^+ + 2e^- \rightarrow H_2$	0
$H_2O + 2e^- \rightarrow 1/2O_2 + 2H^+$	1.23
$CO_2 + e^- \rightarrow CO_2^{\bullet-}$	-1.49
$CO_2 + 2H^+ + 2e^- \rightarrow CO + H_2O$	-0.11
$CO_2 + 2H^+ + 2e^- \rightarrow HCOOH$	-0.20
$CO_2 + 4H^+ + 4e^- \rightarrow HCHO + H_2O$	-0.10
$CO_2 + 6H^+ + 6e^- \rightarrow CH_3OH + H_2O$	0.03
$CO_2 + 8H^+ + 8e^- \rightarrow CH_4 + 2H_2O$	0.17
$2CO_2 + 8H^+ + 8e^- \rightarrow CH_3COOH + 2H_2O$	-0.26
$2CO_2 + 12H^+ + 12e^- \rightarrow C_2H_4 + 4H_2O$	0.07
$2CO_2 + 12H^+ + 12e^- \rightarrow C_2H_5OH + 3H_2O$	0.09
$3CO_2 + 18H^+ + 18e^- \rightarrow C_3H_7OH + 5H_2O$	0.10

In situ and/or operando techniques, along with advanced electrocatalysts rationally designed for CO_2RR, are crucial to gain a deep understanding of the real mechanism of CO_2RR. Therefore, this review summarizes the *in situ* characterization techniques according to fundamental analytic theory and classifies the catalysts by product type. The aim of this review was not to give a detailed illustration of *in situ*/operando characterization techniques selectively used for the CO_2RR system but to illuminate how *in situ* characterization techniques drive the development of CO_2RR and provide some particular examples. This paper would be useful to the scientific community focused on the CO_2RR field, as well as those on materials science and chemistry.

2. Vibrational spectrum analytical techniques

Vibrational spectroscopic techniques, including infrared (IR) and Raman spectroscopies, provide nondestructive, noncontact, and nonvacuum analytical tools to examine the reaction process based on the interaction principles between a vibrational radiation wave and the bond frequencies of the analyzed chemical species.

2.1. Infrared spectroscopy

2.1.1 Basic principles

As a method of absorption spectroscopy, IR band (14300–20 cm^{-1}) radiation is employed to monitor dipole moment changes by exciting the vibrations and rotations of bonds in fragmented molecules, functional groups, and radicals.[9] Transmission, diffusion reflectance, attenuated total reflection (ATR), and reflection–absorption (RA) modes are the most common analytical configurations. ATR and RA are also known as internal and external reflection configurations, respectively. The ATR–IR mode is frequently used in CO_2RR in the interface of a solution and an immobilized catalyst because of its high surface sensitivity and minimized electrolyte layer interference.[10] Absorption intensity is proportional to electric field amplitude and vibrational dipole moment; thus, it can be enhanced by increasing the oscillating electric resonance via the deposition of a thin metallic layer (e.g., Au) on the

crystal plane. This technique is called surface-enhanced infrared absorption spectroscopy (SEIRAS).[11] **Figure 2a** shows an ATR–SEIRAS configuration in an *in situ* CO_2RR system. An incident beam through the high-refraction index crystal undergoes total internal reflection at the waveguide–sample interface, which results in the penetration of an evanescent wave into the sample in the depth of around 0.5–2.0 μm. Interference from solvent absorption can be avoided in this mode. In particular, the surface enhancement effect with a thin metallic film enables the examination of sub-monolayer adsorbates and intermediates on the catalyst surface under *in situ* conditions.[10]

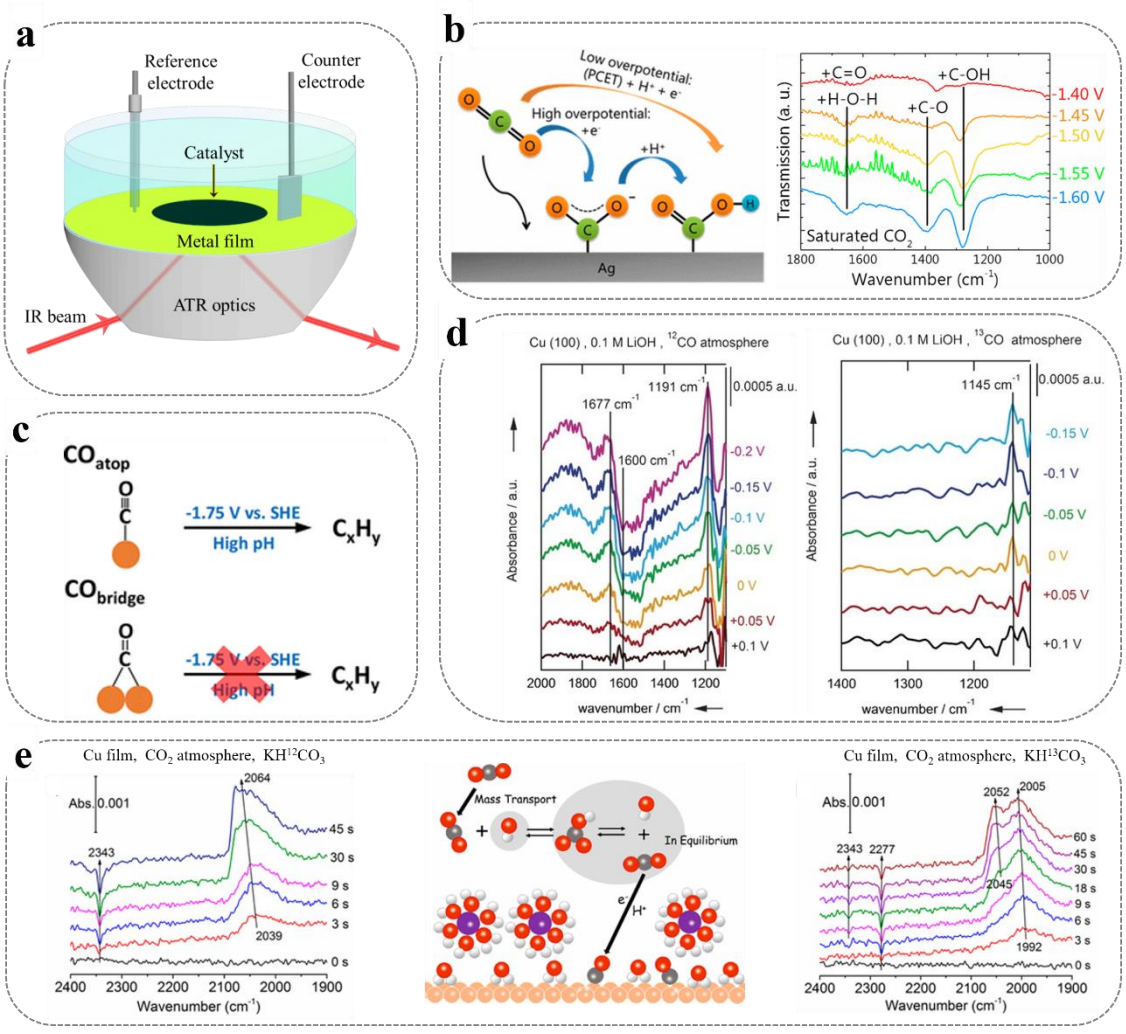

Figure 2. *In situ* FTIR spectroscopy for CO_2RR investigation: a) Schematic of ATR–IR configurations. b) Proposed reaction mechanisms and IR spectra on Ag film. Reproduced with permission.[12] Copyright 2016, American Chemical Society. c) Existence of active and inert *CO intermediates on the Cu electrode. Reproduced with permission.[13] Copyright 2018, American Chemical Society. d) IR spectra for Cu(100) in the presence of ^{12}CO and ^{13}CO. Reproduced with permission.[14] Copyright 2017, Wiley-VCH. e) IR spectra for Cu film in

$KH^{12}CO_3$ or $KH^{13}CO_3$ solutions and schematic of the role of bicarbonate anions in CO_2RR. Reproduced with permission.[15] Copyright 2017, American Chemical Society.

2.1.2 Applications and developments

Product testing and theoretical calculations on several noble metal electrocatalysts indicated that the conversion of CO_2 into carbon monoxide proceeds via the *COOH intermediate, whereas HCOO* is the main intermediate for formate formation.[16] SEIRAS was employed to monitor an intermediate absorbed on pyridine-mediated Pt electrode.[17] The unidentate intermediate *COOH centered at around 1750–1780 cm^{-1} is ascribed to the formation of formate and CO in the presence of pyridine. However, CO is formed in the absence of pyridine. When purged with CO, the absence of *COOH species suggests that proton-coupled electron transfer (PCET) is responsible for the initial formation of *COOH during CO_2RR.[17, 18] According to *in situ* ATR–FTIR on Ag thin films in CO_2RR,[12] the three peaks located at 1288, 1386, and 1660 cm^{-1} can be assigned to the OH^- deformation, C–O stretching, and C=O stretching of *COOH, respectively, at low potentials (Figure 2b). However, the broad and new peaks at 1399 and 1559 cm^{-1} are due to $*COO^-$ intermediate at a high potential (−1.6 V vs. Ag/AgCl), which indicates that individual proton and electron transfer processes occur on Ag instead of the concerted PCET step (Figure 2b).

The three bands on Sn/SnO_x films at 1500, 1385, and 1100 cm^{-1} are assigned to surface-bound $Sn–CO_3$ species. However, the absence of these peaks when the metastable surface oxides are removed reveals the key roles of surface tin oxide species for $Sn–CO_3$ formation.[19] Similar behavior was also observed on indium electrodes.[20] By contrast, the formation of similar metastable oxides on the Pd surface does not enhance the interaction with CO_2 and leads to the reduction of CO_2 to formate.[20b, 21] Notably, CO_2 is reduced directly on the bare metallic surface of Bi without any related oxide.[20b] The results reveal the effect of surface properties on carbon dioxide reduction.[19, 20, 21]

In situ ATR–SEIRAS was performed on Sn-based catalysts to understand the role of surface hydroxyls on metallic oxides in CO_2RR; the intensities of three peaks at 1420, 1370, and 1275 cm^{-1} attributed to HCOO* increased, but the peak at 1498 cm^{-1} attributed to H_2CO_3 decreased with the increase in potential.[22] Discrete Fourier transform (DFT) calculations showed that the moderate surface of Sn–OH is beneficial for CO_2 adsorption in the form of H_2CO_3, which subsequently transforms to HCOO* species to improve HCOOH production.[23]

Cu allows the electrocatalytic reduction of carbon into hydrocarbon and alcohol products with multielectron transfer. In general, multi-carbon products are formed via the formation of surface-adsorbed *CO as the intermediate. Thus, the favorable adsorption of *CO on the Cu surface enables the subsequent reduction into multi-carbon products.[24] The formation of the C–C bond is highly dependent on the adsorption types of *CO intermediates on the surface (Figure 2c).[13] Typically, top-bound *CO is the on-pathway intermediate for multi-carbon products, whereas bridge-bound *CO cannot be activated (Figure 2c). Therefore, the adsorbed status of intermediates can lead to different products.[25] Two peaks at 1191 and 1584 cm^{-1} are speculated as carbon stretching vibrations using isotopically labeled ^{13}CO and D_2O to directly detect hydrogenated *CO dimer on Cu(100) electrodes during CO reduction.[14] These stretching vibrations that originated from C–O–H and C–O were determined as the hydrogenated dimer of OC–COH with the help of DFT calculations (Figure 2d).

Cu oxides and/or oxide-derived copper (OD-Cu) are favorable to produce multi-carbon products in electrochemical CO_2 reduction.[26] The presence of highly active sites on grain boundaries contributes to the remarkable performance of ethanol production on an OD-Cu catalyst.[26a, 27] The enhanced binding of *CO by mitigating σ-interaction due to electron delocalization can improve electrocatalytic activity.[26c] According to the operando ATR–SEIRAS spectra,[26d] in addition to the three bands at 2073, 2089, and 2131 cm^{-1} for *CO adsorption sites, the prominent band at 2058 cm^{-1} on OD-Cu is similar to the adsorption band

of *CO observed on the Cu(100) surface.[28] Thus, the preferable Cu(100) facet will be exposed on the OD-Cu electrode as the typical *CO adsorption site to enhance C–C coupling.

Many efforts have been made to explore the real roles of electrolytes for CO_2RR by *in situ* SEIRAS. Isotopic labeled $^{13}CO_{2(g)}$ and $NaH^{12}CO_3$ solutions were employed on Au electrode to determine the carbon source for carbon monoxide electro-generation.[29] The unlabeled ^{12*}CO peak at 2100 cm^{-1} can be observed initially during CO_2RR, whereas ^{13}*CO (2055 cm^{-1}) is observed only after ~20 min and increases with prolonged time. These results indicate that the equilibrium between bicarbonate (HCO_3^-) and $CO_{2(aq)}$ is involved in the reduction rather than the direct adsorption of $CO_{2(aq)}$. Similar results using isotopic labeled $^{12}CO_{2(g)}$ and $KH^{13}CO_3$ solutions were also observed on Cu electrode by potential-dependent SEIRAS. The peak at 2020–2070 cm^{-1} for *CO was first observed in Ar-saturated $KHCO_3$ solutions (Figure 2e).[15] Therefore, bicarbonate anion plays crucial roles in CO_2RR via the rapid equilibrium exchange with $CO_{2(aq)}$ in the solution instead of only being a pH buffer and proton source.

The cation size of an electrolyte is another key factor that influences activity and selectivity. As early as 1990, alkali metal cations have been proposed to change the selectivity.[30] On the basis of *in situ* SEIRAS,[26b, 31] the reduction of surface-adsorbed *CO will be enhanced with the increase in cations' sizes (Li^+, Na^+, K^+, and Cs^+).[26b, 31a] As the size of cations increases, the increase in pH at the interface during CO_2RR is alleviated,[31b] and the stability of some reaction intermediates is improved by the favorable (electrostatic) interaction with the cation.[31c] These changes are caused by the electrostatic interactions between solvated cations present at the outer Helmholtz plane and the adsorbed species with large dipole moments.[31d] The interfacial pH at different potentials applied to Cu films during CO_2RR was determined using *in situ* SEIRAS by monitoring the labeled bands associated with the pH-dependent equilibrium of $H_2PO_4^-/HPO_4^{2-}/PO_4^{3-}$ ($H_2PO_4^-$, HPO_4^{2-}, and PO_4^{3-} at 1152, 990, and 1010 cm^{-1}, respectively).[31e] The pH was calculated by correlating the ratio of phosphate peaks in

the sample spectra on the basis of the linear combination of phosphate species. At potentials negative than −1.0 V (vs. RHE), the pH near the Cu surface is above 9, which confirms the immense concentration gradients between the electrode surface and the bulk electrolyte. Therefore, the buffer solution is crucial to achieve CO_2RR, which is not favorable in neutral solutions.[31e, 31f]

The development of *in situ* FTIR allows the direct examination of many important intermediates and optimization of reaction conditions for catalytic reactions (Table 2). However, the weak signals of *in situ* FTIR spectroscopy in aqueous-phase experiments result in low signal-to-noise ratios due to the low time resolution to intermediates but high sensitivity of IR light to H_2O molecules. Additionally, the short-life of intermediates makes the identification of various adsorbates at low coverage difficult.

Table 2. Summary of detected *in situ* FTIR bands in CO_2RR.

Electrode	Electrolyte	Band positions (cm^{-1})	Assignment	Ref.
Pd	1 M $KHCO_3$	1583	asymmetric O-C-O	[16a]
		1338	symmetric O-C-O	
		1872	CO_B	
		1977	CO_L	
ZnO	0.1 M $KHCO_3$	~1520-1544	asymmetric O-C-O	[16b]
Pt	0.5 M KCl	1750-1780	$COOH_L$	[17]
Ag film	0.1 M KCl	1559	$*COO^-$ or $COO^{-}*$	[12]
		1288, 1386, 1660	*COOH	
Pt	1 M $KHCO_3$	1950-2000	CO_B	[16c]
		1755-1800	CO_L	
In, Sn, Pb, Bi	0.1 M K_2SO_4	3500, 1650	metal surface oxides	[20b]
In, Sn		1500, 1385	In/Sn-CO_3	
Pb		1410	Pb-CO_3	
Bi		1389	Bi-CO_3	
Sn/SnO_x film	0.1 M K_2SO_4	1500, 1385, 1100	Sn-CO_3	[19]
In	0.5 M K_2SO_4	1459	In-CO_3	[20a]
Sn	0.1 M KCl	1420, 1370, 1275	HCOO*	[22]
		1498, 1435	H_2CO_3	
Cu	0.1 M $NaHCO_3$	2104, 1970	*CO	[24a]

Cu	0.1M LiOH	1191, 1584	OC-COH	[14]
Cu film	0.05 M Li_2CO_3	2000-2100	CO_L	[13]
		1800-1900	CO_B	
Cu	3 M KBr	1100	CH=CO	[25a]
		1400, 1485	CH_2CO	
Pt	1 M $KHCO_3$	1543	*COOH	[25b]
		1495	$(H)CO_3$*	
Cu	1 M $KHCO_3$	1390	$*OCH_3$	[25b]
		1340	$*OCH_2CH_3$	
		1240	symmetric HCOO	
OD-Cu	0.05 M KOH	2058	*CO	[26d]
Cu	0.5 M $NaHCO_3$	2060	*CO	[24b]
Au	0.5 M $NaHCO_3$	2100	$*^{12}CO$	[29]
		2053	$*^{13}CO$	
		1362	$H^{12}CO_3^-$	
		1323	$H^{13}CO_3^-$	
		2343	dissolved $^{12}CO_2$	
		2278	dissolved $^{13}CO_2$	
Cu	0.1 M $KHCO_3$	1720	*CHO	[15]
		2277	$^{13}CO_2$	
		2040	$H^{12}CO_3^-$	
		1990	$H^{13}CO_3^-$	
Cu(100)	0.1 M LiOH	1635-1600	O-H (H_2O)	[31c]
		1191	C-O stretching (OCCOH)	
Cu film	phosphate buffers	1152	asymmetric PO	[31e]
		1076	symmetric PO	
		941	asymmetric POH	

2.2 Raman spectroscopy

2.2.1 Basic principles

As a complementary technique to IR spectroscopy, Raman spectroscopy is widely utilized to characterize the rotational, vibrational, and other low-frequency modes of a sample because of its high selectivity and availability. This technique utilizes a visible light laser for excitation; by measuring the energy differences between incident photons and inelastically scattered photons, information about the vibrational modes of the sample featuring a change

in polarizability can be acquired.[32] Notably, water has low Raman scattering cross-section, so it can be used as the solvent that does not lead to any notable interference to the surface signal; interference raises increasing concerns with operando Raman measurements.

Operando Raman spectroscopy is operated in confocal mode in a chemical reaction cell configuration. One of the key challenges of operando Raman measurements is to improve the limits of detection without distorting electrochemical responses, where the Raman cell plays an important role. After several improvements since 1974,[33] the most common Raman cell in the current CO_2RR field has high numerical aperture (1.0 or 1.1), short working distance, and a water immersion objective lens covered by a thick (13 μm) Teflon film (**Figure 3a**),[34] which can be operated in the electrolyte medium with minimal signal loss. A very large enhancement of the scattered signal can be obtained by using the increase in the electric field intensity at the surface of plasmonic structures, called the surface-enhanced Raman scattering (SERS) effect, to further improve detection sensitivity.[35] In particular, the roughly nanostructured surfaces of Ag, Au, and Cu can give rise to strong surface enhancement under laser excitation; these metals also exhibit high activity for CO_2RR, so they are the most heavily investigated catalysts with SERS spectroscopy.[36] The roughness of metal surfaces is constructed electrochemically by running oxidation and reduction cycles to promote the nucleation process at the interface.[37]

2.2.2 Applications and developments

Operando Raman spectroscopy coupled with electrochemistry is emerging as a powerful tool to study CO_2RR catalysis and has great potential in probing surface changes in catalysts, especially metal oxides, to identify surface-adsorbed intermediates and deduce active sites.

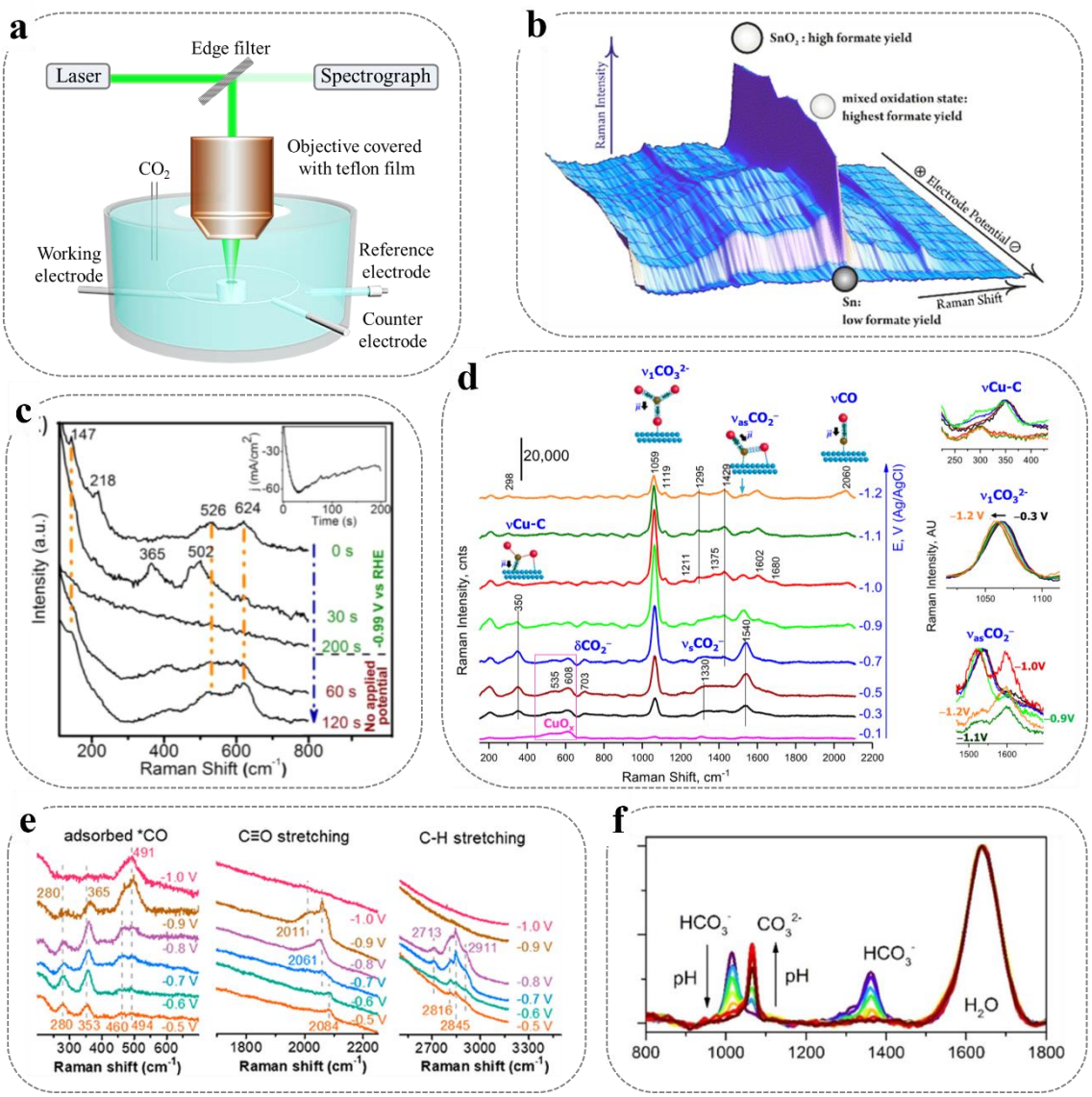

Figure 3. Operando Raman spectroscopy for CO_2RR investigation: a) Schematic of operando Raman configurations. b) Potential-dependent operando Raman spectroscopy related to the oxidation state changes of SnO_2. Reproduced with permission.[38] Copyright 2015, American Chemical Society. c) *In situ* Raman spectra and corresponding chronoamperogram (inset) of Cu film at −0.99 V_{RHE}. Reproduced with permission.[34b] Copyright 2015, American Chemical Society. d) Operando SERS of rough Cu surface in 0.1 M $NaHCO_3$. Reproduced with permission.[39], Copyright 2018, National Academy Sciences. e) Potential-dependent operando Raman spectroscopy of CuAg catalyst. Reproduced with permission.[40] Copyright 2019, American Chemical Society. f) Reference Raman spectra of 0.1 M $KHCO_3$ at different pH values. Reproduced with permission.[41] Copyright 2018, Wiley-VCH.

One application of operando Raman in CO_2RR is to monitor the catalyst state during reaction. SnO_2 has a high selectivity toward formate production.[19, 42] Dutta *et al*. applied potential- and time-dependent operando Raman spectroscopy to monitor the chemical state of

SnO_2 during CO_2RR (Figure 3b).[38] In their observation, three typical bands at 482, 623, and 762 cm^{-1} are assigned to the Eg, A_{1g}, and B_{2g} modes of SnO_2 crystallites, respectively. SnO_2 is the main catalytic species during reduction under moderately cathodic potentials, and the Faraday efficiency (FE) for formate production increases with the decrease in potential until going over a maximum. However, FE is heavily decreased at very negative potentials, where the catalyst is reduced to metallic Sn and results in H_2 generation. Therefore, the highest FE of formate production is at the state where SnO_2 is the main species.

SERS was applied to explore the electrochemical reduction of CO_2 at an Ag electrode in 1995.[43] Since then, an increasing number of SERS studies on Ag catalysts have been performed.[44] For example, Gewirth's group used *in situ* SERS to investigate the beneficial influence of 3,5-diamino-1,2,4-triazole (DAT) on the electrochemical reduction of CO_2 to CO on a silver electrode.[44a] In the absence of DAT, the Raman bands of adsorbed *CO are observed at ~1880 and 1945 cm^{-1}, which are assigned to *CO adsorbed on a threefold hollow site and a bridge site on the Ag surface, respectively. However, two new *CO adsorption peaks at 2049 and 2099 cm^{-1}, which appear in the presence of DAT, are associated with top-bound *CO and physisorbed or weakly coordinated *CO on the electrode surface, respectively, where the bands at ~1880 cm^{-1} disappear. Thus, the addition of DAT can block the sites of more stable CO coordination and increase the efficiency of Ag–DAT because of the enhanced CO removal.

Operando Raman technology has been widely used to monitor the surface states of copper catalysts, where copper is the most promising catalyst for producing multi-carbon products.[34b, 34c, 34d, 45] For instance, Ren *et al.* employed time-dependent *in situ* Raman to investigate the surface states of Cu_2O film during CO_2RR (Figure 3c).[34b] Four bands attributed to the vibrational fingerprints of Cu_2O were detected at 147, 218, 526, and 624 cm^{-1} at the start of reduction (at 0 s) but attenuated along with the appearance of two new bands at 365 and 502 cm^{-1} after 30 s. This finding demonstrates the rapid reduction of top Cu_2O film

layers. The detected Cu–O vibrations belong to intermediately reduced Cu oxides. No peaks could be observed in the Raman spectrum from 200 s onward. This result indicates that the Cu_2O films were reduced thoroughly and remained as metallic Cu^0 particles during CO_2 reduction. A similar phenomenon was observed in other studies[34c, 34d] even with different surface morphologies and crystal orientations.[45] Interestingly, Yu's group recently reported that the Cu_2O catalyst with nanocavities can confine intermediates formed *in situ*, which in turn covers the local catalyst surface and prevents Cu^+ from being reduced to Cu^0 to some extent.[46]

Although many Raman spectroscopic studies have detected the bound product, "absorbed CO," on metal surfaces, the first common reaction intermediate, $*CO_2^-$, proposed by Hori *et al*. has not been investigated. Chernyshova *et al*. explored a roughened Cu electrode by one oxidation–reduction cycle to identify the structure of this intermediate using potential-dependent SERS (Figure 3d).[39] They first concluded that the peaks at 1540 and 350 cm^{-1} characterize the same species because of their coincident changes in all potentials. The peak at 1540 cm^{-1} is assigned to the $\nu_{as}(CO_2^-)$ vibration of η^2(C,O)-CO_2^- and that at 350 cm^{-1} is assigned to the adsorbate surface vibration of ν(Cu-C) in η^2(C,O)-CO_2^- with the help of isotope labeling experiments and DFT calculations. Given that the intensity of this intermediate is fully consistent with the potential for producing formate and CO, $*CO_2^-$ is a common intermediate of formate and CO formation during CO_2RR. The intermediate of *COOH was detected by *in situ* Raman technology.[47]

Operando Raman or SERS technology has recently provided indications for copper-based bimetallic or alloy catalysts.[40, 48] For instance, Gao *et al.* applied potential-dependent SERS on Cu–Ag bimetallic and Cu catalysts to investigate the mechanism of the high production of C_{2+} products in 0.1 M $KHCO_3$ (Figure 3e).[40] In addition to the common peaks (282, 355–366, and 2057–2092 cm^{-1} for *CO on Cu, Cu–CO stretching, and C≡O stretching, respectively) on Cu–Ag and Cu catalysts, new bands assigned to *CO on Ag (460, 491–494, and 2011 cm^{-1})

and CH-containing intermediates (2713 and 2816 cm^{-1}) appeared on the Cu–Ag catalyst and provided evidence for the suggestion that the desorbed *CO on Ag spills over to Cu sites and that on Cu undergoes further reduction. Thus, the Cu–Ag catalyst delivers improved activity toward the formation of C_{2+} products. Same conclusions were drawn by other studies.[48c, 48j] Sargent's group attributed the high FE of ethanol on Ag/Cu catalyst to the diversity of binding sites,[48f] whereas others ascribed the improved product selectivity to synergistic effect[48b, 48g] or charge redistribution on bimetallic catalysts.[48e, 48h]

Beyond the specific transformation of materials and the detection of intermediates, operando Raman spectroscopy can also be employed to monitor reaction environments.[41, 49] Klingan *et al*. investigated the local interfacial pH on porous Cu films by monitoring the band intensities of HCO_3^- and CO_3^{2-} through time-dependent operando Raman spectroscopy (Figure 3f).[41] In calibrated solutions, the HCO_3^-/CO_3^{2-} equilibrium generally shifted toward CO_3^{2-}, the peaks at 1015 and 1363 cm^{-1} (HCO_3^-) decreased, and the peak at 1065 cm^{-1} (CO_3^{2-}) increased as the pH increased. Nevertheless, in real-time monitoring, the local interfacial pH is 9.0 at −0.6 V_{RHE} and even higher than 10 at −0.7 V_{RHE}. The drastic increase in local pH is likely related to the diffusion limitations of HCO_3^- ions acting as proton carriers, which is analogous to the role of $H_2PO_4^-$ revealed by SEIRAS.[31e]

Simliar to *in-situ* FTIR, operando Raman spectroscopy can provide valuable information about reaction intermediates during CO_2RR on the basis of chemical structure analysis (Table 3). This optical technique is highly dependent on the intrinsic vibrational, rotational, and other modes in molecules under the inelastic scattering of monochromatic light. Therefore, Raman spectra are only suitable to the electrocatalyts with chemical functional groups that scatter light at different frequencies.

Table 3. Summary of detected operando Raman bands in CO_2RR.

Electrode	Electrolyte	Band positions (cm^{-1})	Assignment	Ref.
SnO_2	0.5 M NaOH	482, 623, 762	E_g, A_{1g}, B_{2g} of SnO_2	[38]
Ag	1 M KOH + $Ca(OH)_2$	1014, 1355	HCO_3^-	[44a]

		685, 1049	CO_3^{2-}	
		284, 392, 722, 1500	Ag-CO_3^{2-}	
		2044-2051	atop-bound CO	
		1838-1950	bridge-bound CO	
		1815-1870	3-fold hollow CO	
Ag	0.1 M $KHCO_3$	1625	O-C-O antisymmetric stretch	[43]
		1390	C-H bending	
		1360	O-C-O symmetric stretch	
Cu_2O film	0.1 M $KHCO_3$	147, 218, 526, 624	Cu_2O (vibrational fingerprints)	[34b]
		365, 502	Cu-O vibrations	
Cu_xZn film	0.1 M $KHCO_3$	430, 560	ZnO	[34c]
CuS_x	0.1 M $KHCO_3$	295	Cu-S stretching	[34d]
		~470	S-S stretching	
		2080	*CO (C≡O stretching)	
		356	Cu-CO stretching	
		275	*CO (C≡O frustrated rotation)	
rough Cu	0.1 M $NaHCO_3$	2050-2070	*CO (C≡O stretching)	[39]
		~280	Cu-CO frustrated rotation	
		360	Cu-CO translation	
		~1065	$v_1CO_3^{2-}$ (symmetric C-O)	
		1540	$v_{as}CO^{2-}$ (η^2(C,O)-CO^{2-})	
		350	vCu-C (η^2(C,O)-CO^{2-})	
Cu_2O/ CuO@Ni	0.5 M $KHCO_3$	3350	H-O-H bending	[47]
		1064	HCO_3^-	
		1640	COOH*	
CuAg	0.1 M $KHCO_3$	460, 491-494, 2011	Ag-CO	[40]
		2713, 2816	CH-containing intermediates	
AgCu film	0.1 M $KHCO_3$	419	Ag-O	[48b]
		304, 2848, 2906	$HCOO^-$ or HCOOH	
Cu-Sn alloy	0.1 M $KHCO_3$	1295	C-OH stretching (*COOH)	[48e]
		1436	C-O stretching (*COOH)	
		1635	C=O asymmetric (*COOH)	
		1390	symmetric stretch of *OCHO	

3. X-ray-based analytical techniques

X-rays can be applied as an analytical tool to supplement the limitations of vibrational analytical techniques. Different phenomena, such as absorption and scattering, which are

useful for the quantitative or qualitative analysis of materials, can occur because of the interaction between X-rays and matter. Since the advent of third-generation high-energy synchrotron, extremely bright and high-energy X-rays bring huge advantages for *in situ*/operando studies in catalytic reactions. In the next section, two analytical techniques, namely, X-ray absorption spectroscopy (XAS) and X-ray photoelectron spectroscopy (XPS), are introduced.

3.1 X-ray absorption spectroscopy

3.1.1 Basic principles

XAS is a highly effective and powerful technique for the investigation of the coordination structure of electrode materials; it provides elemental information in local environments according to the X-ray absorption coefficient as a function of incident X-rays. XAS is element specific and sensitive to extremely low concentrations (i.e., 10-100 particle mol^{-1}); thus, it can analyze crystalline and amorphous nanostructures. During XAS, core electrons can be excited by photon energies in the wide range of 50–100 keV. Specifically, X-ray with energy between 50 and 2000 eV is called soft XAS, which covers the K-edge of light elements and the L-edge of 3d transition metals. Hard XAS with energy up to 100 keV is divided into two parts: X-ray absorption near edge structure (XANES) and extended X-ray absorption fine structure (EXAFS).[50] The XANES region, as the part of the spectrum near the absorption edge, is strongly sensitive to the oxidation state and coordination structure of the absorbing atoms; the EXAFS region has been largely exploited to gain quantitative structural information, such as coordination number and coordination shell distance, from the absorbing atoms.[51]

Transmission, fluorescence, and electron yield modes are the three basic modes for *in situ*/operando XAS signal collection (**Figure 4a**). Among them, the transmission mode detects concentrated and homogenous samples by measuring the intensity differences between incident and transmitted X-rays. The fluorescence mode, which can detect the X-rays emitted by elements, can analyze diluted and non-homogenous samples. The emitted photoelectrons

can also be measured by the electron yield mode. Notably, the electron yield mode is surface sensitive because of the relative short mean free path of photoelectrons, whereas the two other modes are bulk-sensitive.[52]

3.1.2 Applications and developments

XAS has been used in probing oxidized states and investigating element sites in the crystal lattice and atomically dispersed structures. Thus, it is convenient for monitoring catalyst stability and identifying catalytically active sites during chemical reactions.

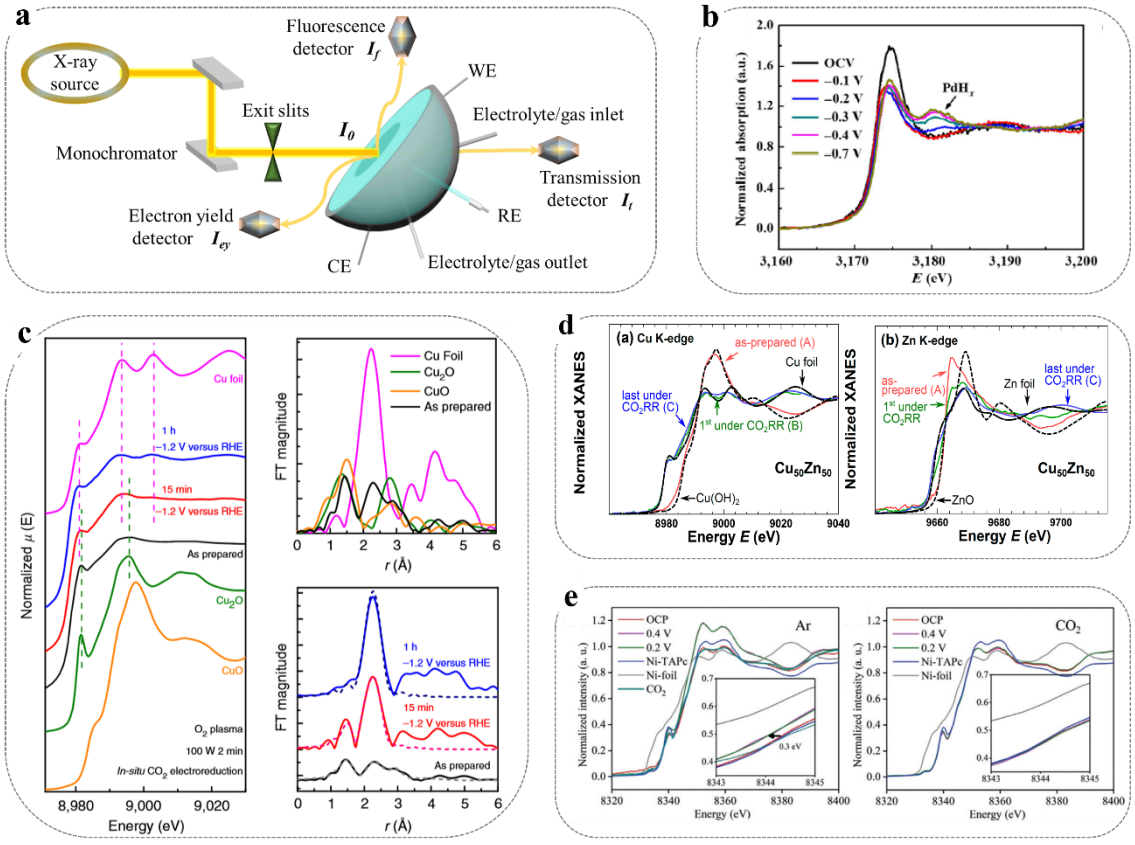

Figure 4. Operando XAS for CO_2RR investigation: a) Schematic of the experimental setup for the three different operando/*in situ* XAS detection modes: transmission, fluorescence, and electron yield modes. b) *In situ* Pd L_3-edge XANES spectra at different applied potentials. Reproduced with permission.[16a] Copyright 2017, Tsinghua University Press. c) XANES and EXAFS spectra of plasma-treated copper sample under operando conditions. Reproduced with permission.[53] Copyright 2016, Nature Publishing Group. d) Cu and Zn K-edge XANES spectra of $Cu_{50}Zn_{50}$ nanoparticles at different times under CO_2RR conditions. Reproduced with permission.[54] Copyright 2019, American Chemical Society. e) Normalized Ni K-edge XANES spectra of Ni-CNT-CC acquired at various applied potentials (vs. RHE) under electrocatalytic reaction conditions. Reproduced with permission.[55] Copyright 2020, Wiley-VCH.

Similar to operando Raman technology, *in situ* XAS can also be used to monitor structural information during CO_2RR.[56] As reported first on Zn catalyst, chemical oxidation (Zn^0 to Zn^{2+}) occurs at more positive potentials than −0.7 V, whereas nanostructured Zn catalysts are structurally stable and remain at Zn^0 state at potentials lower than −0.7 V.[57] Unlike metallic Zn, Ag and Sn species are easily oxidized into metal oxides in air and also easily reduced to metal states when negative potentials are applied. Although most oxides are reduced at the beginning of CO_2RR, a few oxides are still preserved to some extent at the end.[57a, 57b] In addition, when Sn is modulated by S, an oxidation state between Sn^0 and Sn^{2+} is observed by *in situ* Sn L_3-edge spectra even after reducing SnS_x to Sn(S) at −0.7 V (vs. RHE), whereas Sn nanoparticles are kept at the Sn^0 state.[57c] These findings confirm that increasing the number of uncoordinated Sn sites in Sn(S) improves the FE of formate production in CO_2RR.

The active phase on Pd-based electrocatalysts can also be monitored by *in situ* XAS.[16a, 58] The systematic engineering of the active phase in Pd nanoparticles by *in situ* Pd K and L_3-edge XAS measurements from −0.1 V to −0.7 V (Figure 4b)[16a] revealed that the Pd–Pd interatomic distance remarkably increases (from 2.75 Å to 2.81 Å) as the potential shifts negatively from open circuit potential (OCP) to −0.7 V because of the formation of palladium hydride (PdH_x) via the insertion of hydrogen atoms into the Pd lattice. The new peak at ~3181 eV in the Pd L_3-edge spectra further confirms the absorption of hydrogen atoms on bulk Pd. Through DFT calculations, the mixed PdH_x with α and β phases facilitates formate production, whereas β-PdH_x promotes CO production. Chen's group also confirmed this result[58a] and verified that the single-atom Pd active site in the Pd–N_4 structure coordinated by four N atoms can facilitate CO production with the oxidation state of Pd between 0 and +2.[58b]

For Cu-based catalysts, except for exploring the reaction intermediates and surface states by *in situ* IR and Raman spectroscopies, *in situ* XAS can be utilized to track the transition in surface chemical states during CO_2RR.[41, 45b, 59] The Cu L_3-edge was selected to track in real time the transition of Cu oxidation states with the potential applied.[59a] Typically, the peak at

931 eV associated with Cu^{2+} decreases, whereas another higher-energy peak around 934 eV assigned to Cu^{+} begins to emerge at the applied potentials from a more positive potential to 0.28 V; this finding suggests the transition from Cu^{2+} to Cu^{+}. Time-dependent XAS spectra show the rapid structural change from Cu^{2+} to Cu^{+} within 5 min at 0.28 V (vs. RHE) and the complete transition from Cu^{+} to Cu^{0} at the more negative potential of −1.87 V (vs. RHE). Furthermore, Kauffman's group indicated the onset potential of Cu oxide reduction at −0.2 V (vs. RHE); no remarkable signatures associated with oxides under operating conditions were observed at −0.6 V (vs. RHE).[45b]

Cu^{+} promotes C_{2+} production because of easy CO_2 activation and C–C coupling;[60] thus, monitoring and keeping the stability of Cu^{+} state are important.[53, 61] Mistry *et al.* investigated the changes in the oxide layer on a plasma-treated Cu electrode at −1.2 V (vs. RHE) using time-dependent operando XAS (Figure 4c).[53] The XANES spectra exhibit the features of Cu_2O with a prominent shoulder at ~8,982 eV, and the EXAFS data show the coexistence of metallic Cu and Cu oxide in the initial sample. After 1 h of reaction, only metallic Cu features are discernable in the EXAFS spectrum, whereas an oxygen content of 25%–28% can be observed on the surface layer by scanning transmission electron microscopy (TEM) coupled with energy-dispersive X-ray spectroscopy; thus, the oxides on the surface layer are surprisingly stable after 1 h of reaction at relatively high potentials. Chen's group explored the effects of Cu_2O thickness coated on Ag nanowires via *in situ* XAS.[61a] They confirmed that the oxidation of Cu^{0} in aqueous electrolyte governs the chemical state of active Cu centers, and a dynamic equilibrium between Cu^{0} and Cu^{+} can be reached under mild conditions because of the trace amount of oxidative species in the electrolyte.

The structure and composition of bimetal catalysts under working conditions can also be monitored by operando XAS.[54, 62] For example, the application of time-dependent operando XAS on bimetallic CuZn catalyst revealed changes in the crystallographic structure (Figure 4d).[54] Initially, the operando Cu and Zn K-edge XANES spectra of the $Cu_{50}Zn_{50}$ sample

indicate that Cu and Zn components are completely oxidized and predominantly in the +2 oxidation state. Interestingly, the reduction rates appear to be very different under CO_2RR conditions; the reduction of ZnO species takes several hours, whereas that of Cu oxide species is completed during the first XAS scan within several minutes. The results of the Fourier transform–EXAFS spectra of Cu K-edge show that the Cu–M (M=Cu or Zn) interatomic distance (2.58 ± 0.01 Å) is in between that of a Cu foil (2.56 Å) and a brass CuZn foil (2.62 Å), which suggests the gradual alloying between Cu and Zn atoms under CO_2RR conditions.

Ni single-atom catalysts (SACs) are one of the promising electrocatalyst candidates for CO_2-to-CO conversion, and catalytically active sites are widely identified by operando XAS experiments.[55, 63] As reported,[55] the Ni K-edge XANES spectra under cathodic potential showed that the shift of ~0.3 eV to a lower energy would stem from the reduction of Ni species in Ni-TAPc/CNTs, possibly Ni^{2+} to Ni^{+}, thereby activating CO_2 molecules via the donation of lone pair electrons (Figure 4e). Moreover, the electronic structures of active center single atoms can be monitored by operando XAS.[63c, 64] Specifically, as shown in the Ni K-edge EXAFS spectra of an atomically dispersed nickel catalyst on nitrogenated graphene,[63c] the shift to approximately 0.4 eV higher energy in CO_2-saturated $KHCO_3$ solution under OCP bias compared with that in Ar-saturated condition indicates an increase in Ni oxidation state, which results from the delocalization of unpaired electron in the $3d_{x^2-y^2}$ orbital and the spontaneous charge transfer from Ni^{+} to the carbon 2p orbital in CO_2 to form a $CO_2^{\delta-}$ species. These processes help reduce the energy barrier for electrochemical CO_2 reduction.

In addition to Ni SACs, other metal atomic catalysts, such as Zn, Cu, and Co, can be used in CO_2RR.[65] The first Zn-based molecular catalyst with high product selectivity in CO_2 reduction was reported by Wu *et al*.[65a] *In situ* XAS revealed that the Zn(II) center at the prepared heterogenized zinc–porphyrin complex catalyst maintains its oxidation state from OCP to −1.7 V (vs. SHE), indicating a redox-innocent characteristic. However, Cu SACs

show a different phenomenon.[65c, 65d] As reported in the Cu K-edge XANES spectra,[65d] the catalyst copper(II) phthalocyanine (CuPc) shows a characteristic Cu(II) peak at ~8985 eV under OCP conditions. As the potential decreases to −0.66 V (vs. RHE), a small absorption peak associated with Cu(I) appears at ~8981 eV, and another peak at ~8980 eV, which corresponds to Cu(0), starts to develop at −0.86 V (vs. RHE). Notably, upon switching the electrode potential back to 0.64 V, the Cu(0) peak disappears and the XANES spectrum is almost restored to the initial status at the OCP, confirming its excellent reversibility.

In situ XAS based on synchrotron radiation can provide valuable information about the electronic, structural, and magnetic properties of certain elements in the electrocatalysts for CO_2RR (Table 4). Such data are helpful to understand the catalytic nature of an electrocatalyst. Nevertheless, *in situ* XAS can only describe the average information on local structures due to its bulk sensitivity and rigorous operation conditions including ultrahigh photon energy, which makes its use for component analysis of complex systems rather difficult.

Table 4. Summary of *in situ* XAS data under various CO_2RR conditions.

Electrode	Electrolyte	Binding energy (eV)	Apparent distance (Å)	Ref.
Zn	0.5 M $NaHCO_3$	-	~2.3 (Zn-Zn)	[11]
		-	1.55, 2.03 (amorphous Zn oxide)	
$Sn_{2.7}Cu$	1 M KOH	-	1.5~2.0 (Sn-O)	[57b]
Pd SAC	0.5 M $NaHCO_3$	-	~1.5 (Pd-N)	[58b]
Pd NPs	1 M $KHCO_3$	-	2.75 (Pd-Pd)	[16a]
		~3181 (PdH_x)	2.81 (PdH0.5)	
Pd NPs	0.5 M $NaHCO_3$	-	2.748 (Pd-Pd)	[58a]
		-	2.818, 2.842 (PdH)	
Cu nanoneedle	0.1 M $KHCO_3$	931 (Cu^{2+})	-	[59a]
		933 (Cu^{+})	-	
CuO-IO	0.1 M $KHCO_3$	-	1.53 (Cu-O in CuO)	[45b]
		-	2.52 (Cu-Cu in CuO)	
		-	2.21 (Cu-Cu in metallic Cu)	
CuCat	0.1 M $KHCO_3$	-	1.92 (Cu-O, Cu^{2+})	[41]
		-	2.51, 3.58, 4.41 (Cu-Cu in metallic Cu)	
Ag@CuO_x	0.1 M $KHCO_3$	8982, 8995 (Cu_2O)	~1.5 (Cu-O in Cu_2O)	[61a]

		-	2.7 (Cu-Cu in Cu_2O)	
		-	~2.2 (Cu-Cu in metallic Cu)	
CuZn bimetallic NPs	0.1 M $KHCO_3$	-	2.56 (Cu-Cu in Cu foil)	[54]
		-	2.62 (CuZn foil)	
		-	2.56-2.62 (Cu-Zn alloy)	
Ni-NG	0.5 M $KHCO_3$	-	~2.2 (Ni-Ni in NiO)	[63b]
		-	1.62 (Ni-O in NiO)	
		-	1.40 (Ni-N in Ni-Pc)	
		-	2.06 (Ni-Ni in Ni clusters)	
Ni-NG/Ni foil	0.5 M $KHCO_3$	-	2.15 (Ni-Ni)	[63c]
A-Ni-NG		-	1.45 (Ni-N)	
A-Ni-NSG		-	1.81 (Ni-S)	
(Cl, N)-Mn/G	0.5 M $KHCO_3$	-	1.63 (Mn-Cl/N)	[64b]
		-	1.49 (Mn-N in Mn-N_4)	
		-	~2.3 (Mn-Mn)	
		-	2.6 (Mn-C)	
CuPolyPc@CNT	0.1M $CsHCO_3$	8983.93 (Cu^{2+})	1.5 (Cu-N in Cu-N_4)	[65c]
		8979.2 (Cu metal)	8979.2 (Cu metal)	

3.2 X-ray photoelectron spectroscopy

3.2.1 Basic principles

XPS has been developed to determine surface compositions, oxidation states, and electronic structures with high surface sensitivity.[66] This method analyzes excited core electrons, whose binding energies are specific to elements. Thus, the "chemical shifts" for specific peaks allow the identification of local chemical environment and electronic structure.[66a] Spectroscopic experiments are typically performed in an ultrahigh vacuum (UHV) chamber, which limits *in situ* applications under ambient conditions, especially in the presence of gases and liquids, because of the short penetration length of X-rays in ambient atmosphere (~10 mm).[67] Since the advent of third-generation synchrotron light sources, two types of *in situ* measurement setups via ambient pressure XPS (APXPS) have been developed to focus on realistic pressure: (I) differentially pumped analyzer and (II) membrane based setup.[68]

Figure 5a shows a schematic of the *in situ* electrochemical APXPS setup. In mode I, the sample is exposed to elevated pressure (mbar range) while maintaining a high vacuum ($<10^{-6}$ mbar) in the hemispheric analyzer with several differential pumping stages; the cone with a narrow aperture is situated very close to the sample surface to collect photoelectrons before they are scattered by gas molecules. In mode II, the sample is placed inside a membrane tightly covered cell, in which the membrane separator between the outer vacuum and inner ambient is electron transparent but gas/liquid/solid (molecular) impermeable (typically Si microchip-supported Si_3N_4 film, 10–15 nm).[69] Mode I is applied only to study electrochemical processes at solid–vapor interfaces, whereas mode II is applied to solid–liquid interfaces.[66b]

3.2.2 Applications and developments

Unlike XAS, which can be used to analyze the oxidizing status and bulk structure of samples, (quasi) *in situ* XPS techniques with surface sensitivity have been widely used to characterize the valence change of elements and the electron transfer processes on the active sites of a catalyst during chemical reactions to provide deep insight into the design of high-performance catalysts.

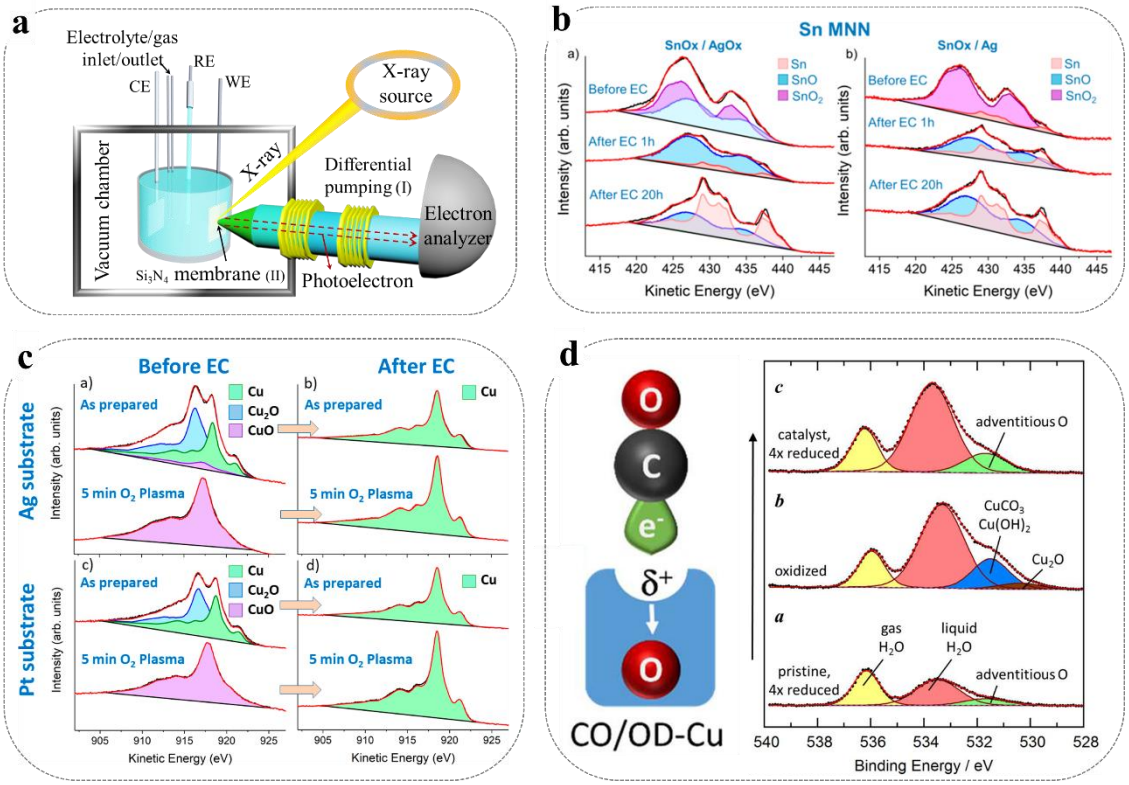

Figure 5. ***In situ*** **XPS spectroscopy for CO_2RR investigation:** a) Schematic representation of *in situ* electrochemical APXPS setup. b) Quasi *in situ* Sn MNN Auger spectra of SnO_x/AgO_x and SnO_x/Ag samples. Reproduced with permission.[70] Copyright 2019, American Chemical Society. c) Quasi *in situ* Cu LMM XPS spectra acquired on Ag- and Pt-supported Cu dendrites before and after 1 h of CO_2RR. Reproduced with permission.[71] Copyright 2019, American Chemical Society. d) *In situ* O 1s APXPS spectra in Cu foil under different conditions. Reproduced with permission.[72], Copyright 2016, American Chemical Society.

Quasi *in situ* XPS measurements were performed to monitor the surface status of the catalysts at a depth of approximately 5 nm.[57a] For example, the O_2 plasma-treated silver sample showed a binding energy of 367.5 eV due to the formation of Ag oxide. The oxide can still be detected in the initial reaction process but disappears rapidly in 3 min. Thus, metallic Ag is responsible for the long-term operation of the catalytic process. Moreover, the O_2–plasma treatment of tin electrodeposited on silver films, namely, SnO_x/AgO_x, aimed to reveal the effect of the chemical state and composition of a catalyst on the activity and selectivity of the films.[70] Surprisingly, SnO_x species progressively decreased with the increase in reaction time. However, the observed tin oxides on the surface even after 20 h of CO_2RR (Figure 5b) contributed to the enhanced activity and stable selectivity of CO/formate.

Besides *in situ*/operando Raman and XAS technologies, the transition of the surface chemical states of Cu oxide catalysts can also be examined by quasi *in situ* XPS measurements.[41, 71, 73] The Cu dendrites grown on Ag and Pt foils via electrodeposition exhibit the co-existence of Cu and Cu oxides[71] (Figure 5c). Cu dendrites can be transformed into CuO via oxygen plasma treatment, but Cu_xO species are reduced during CO_2RR at an applied potential of −0.9 V (vs. RHE). This result indicates the lack in stability of Cu_xO species.

Although copper oxide electrocatalysts will be reduced during CO_2RR, residual oxygen under the subsurface can be observed.[72, 74] For example, *in situ* APXPS technology was used to detect the oxygen states of copper foils under different conditions.[72] A small adventitious oxygen peak at 531.7 eV was observed in pristine copper foil after removing surface oxides (Figure 5d). Adventitious oxygen is substituted by two components, namely, $CuCO_3$/$Cu(OH)_2$ and Cu_2O, after oxidation. Interestingly, the adventitious oxygen peak shows a substantially increased intensity compared with the initial spectrum before oxidation. Thus, combined with the electron energy-loss spectra, the results revealed that adventitious oxygen will increase the CO binding energy on the catalyst by reducing σ^- repulsion and facilitate C–C bond formation because of the improved CO coverage on the catalyst.

Compared with *in situ* XAS, *in situ* XPS can hardly examine the alloying process.[54, 75] As described above, the transition from bimetallic CuZn catalyst into CuZn alloy before and after CO_2RR has been revealed by operando XAFS.[54] However, from the quasi *in situ* XPS spectra, the binding energy for Cu $2p_{3/2}$ exhibits a transition from Cu^{2+} into metallic Cu, whereas the Zn $2p_{3/2}$ spectrum reveals the presence of $Zn(OH)_2$ after the reaction. Meanwhile, the sample composition is consistent with the molar ratio of precursors even after CO_2RR. In addition to liquid electrolytes, the electrolytic behavior of solid oxide is often studied by near-ambient pressure XPS to detect reaction intermediates and understand mechanistic information.[76]

On the basis of the chemical shift, the changes in valence states and coordination environment of the specific element can be precisely analyzed by *in situ* XPS. However, this surface-sensitive technique with limited detection depth cannot easily reveal the internal changes of bulk electrocatalysts. Additionally, the high-vacuum degree is a major hinder to implement such a technique for operando reactions.

4. Mass spectrometry

4.1 Basic principles

Mass spectrometry (MS) is an analytical technique that uses pervaporation to continuously separate and collect reaction products. The analysis time of MS is approximately a second; thus, the generation rates of gaseous and/or volatile reaction products can be semi-quantified in real time by recording the partial ion current densities of reaction products. For *in situ* electrochemical MS, an electrochemical cell is coupled with a mass spectrometer to detect the gaseous products in real time by placing a sampling tip close to the electrode surface.[77] However, online electrochemical mass spectrometry (OLEMS) has extremely low collection efficiency and is highly sensitive to the distance between the sampling tip and the electrode surface. It is incapable of detecting the liquid-phase products of CO_2RR or quantifying any reaction products in real time.

Differential electrochemical mass spectrometry (DEMS) was developed using a vacuum system with two pumping stages to sample for MS measurement (**Figure 6a**). For the simple principle of the setup,[78] a porous hydrophobic Teflon membrane is placed between the electrochemical cell and a differentially pumped MS, and the species ionized by electron impact can be separated according to the mass-to-charge (m/z) ratio by a quadrupole mass analyzer. In DEMS, the electrolyte flow (commonly ~1 μL s^{-1}) is crucial to maintain the mass transfer of CO_2 at the cathode. A pressure below 10^{-5} Torr is maintained via two turbomolecular pumps to keep the DEMS system in near vacuum condition. This method has

a very short response time and provides a tool for the detection of gaseous- and liquid-phase products.

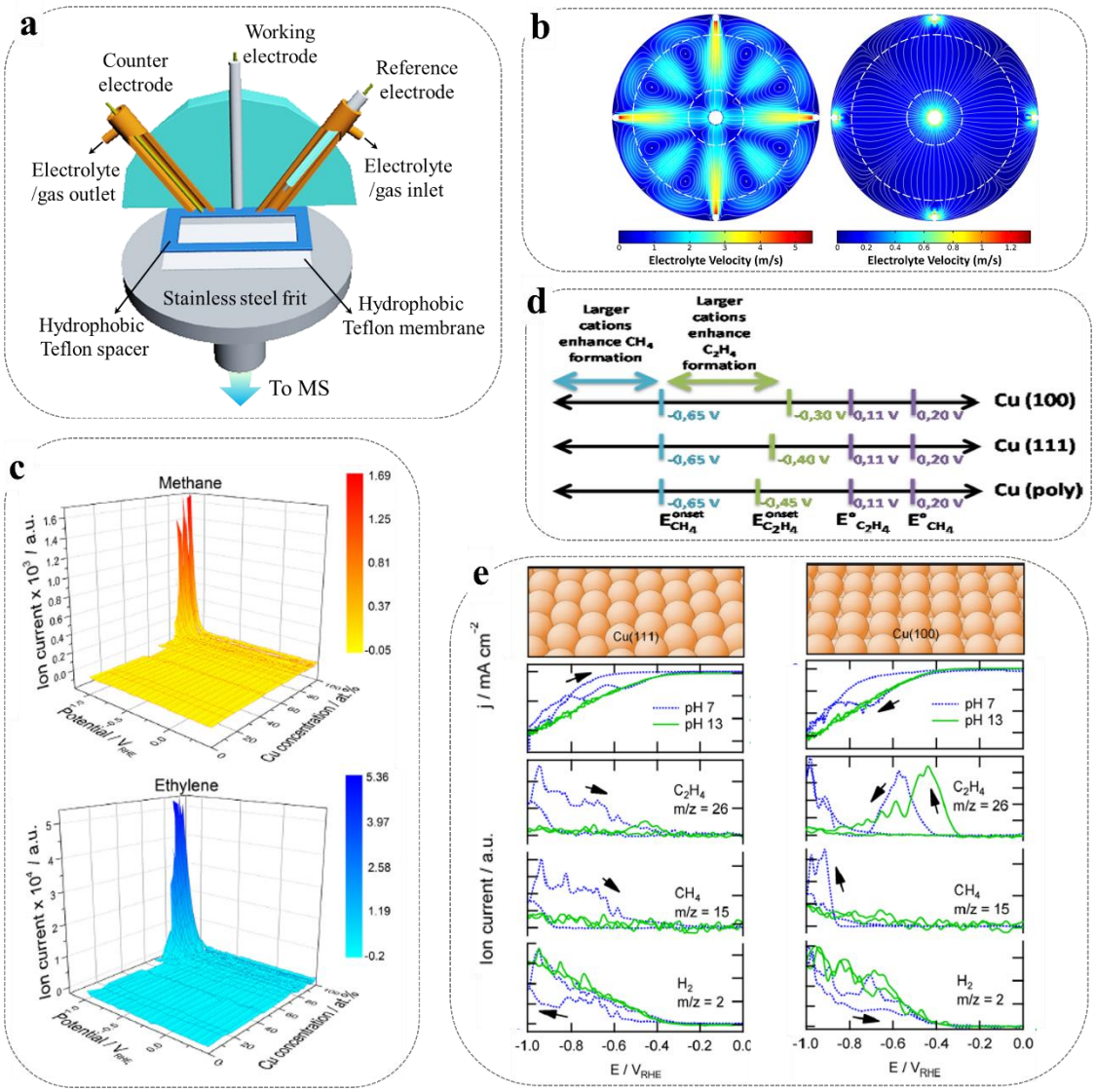

Figure 6. Mass spectrometry for CO_2RR investigation: a) Schematic of DEMS cell. b) Catholyte flow field in the working electrode chamber at a flow rate of 1 mL min^{-1} for convection driven by pressure at the inlet and outlet. Reproduced with permission.[80] Copyright 2015, American Chemical Society. c) MS signals for potential sweep experiments on the potential dependence and composition of Cu–Co thin film samples. Reproduced with permission.[81] Copyright 2016, Elsevier. d) Schematics of the structure- and potential-dependent cation effects for CO reduction toward methane and ethylene in alkaline hydroxide electrolytes. Reproduced with permission.[31c] Copyright 2017, American Chemical Society. e) Cyclic voltammograms and MS signals for CO reductions on the Cu(111) and Cu(100) facets in PBS and NaOH solutions. Reproduced with permission.[82] Copyright 2012, American Chemical Society.

4.2 Applications and developments

The immediate detection of electrochemical reaction products is crucial for product analysis. MS enables the identification of products and/or intermediates during continuous faradaic reactions and the characterization of adsorbates on polycrystalline and single-crystal electrode surfaces via their desorption.[79]

MS permits the concurrent detection of products following potential and time, which gives molecular specificity.[83] Koper and co-workers developed an OLEMS capable of detecting the hydrocarbon products of CO_2RR in real time using a sampling tip placed in close proximity with the electrode surface.[77a] Mayrhofer's group then designed an online MS coupled with a miniaturized electrochemical scanning flow cell for the determination of reaction products dependent of the applied potential and/or current regime, as well as the fast and automated changes in the sample.[77b] As demonstrated by the OLEMS measurements, the onset potential for generating CO on the Au(110) surface with high selectivity is lower than those on Au(111) and Au(100); thus, CO_2RR is dependent on the surface atomic arrangement of Au(hkl) electrodes.[83e]

Furthermore, Bell and co-workers reported a novel DEMS cell geometry that enables the partial current densities of volatile electrochemical reaction products to be quantified in real time (Figure 6b); their work is the first to report on the transient selectivity of CO_2RR to C_{2+} liquid-phase products.[80] Recently, a new electrochemical real-time MS approach was used to determine the products on pristine and *in situ*-anodized copper during potential step or sweep experiments. The enhanced formation of several C_{2+} products over C_1 products is tracked directly after copper anodization with unprecedented temporal resolution, which creates new opportunities for resolving processes that occur at short timescales and eventually for guiding the design of new, robust catalysts for CO_2RR.[84]

Similarly, the reduction of copper oxides during CO_2RR can be detected by *in situ* MS.[45a, 85] In an alloy catalyst of Cu–Co thin film with changing Co atomic ratio from 5% to 15%, ethylene evolution dominates and precedes methane production and is beneficial for forming

C_2 products (Figure 6c).[81] The hydrogen evolution reaction is dominant over CO_2RR for high Co concentrations. Furthermore, the effects of cations on CO reduction on Cu(100), Cu(111), and Cu-(polycrystalline) electrodes are discussed in detail in Figure 6d.[31c] Larger cations are associated with the higher selectivity of the major products of methane and ethylene. However, for onset potential, the formation of ethylene depends on cations and exposed crystal faces, whereas methane depends only on cations.

Although the underlying mechanisms of CO_2RR into multi-carbon products over various catalysts are not easy to examine,[6, 82, 86] the dynamic identification of products, including formate, methanol, and ethanol, has become possible through DEMS.[86a] The formation pathways of formate are different from those of methanol and methanal, and *CO is the intermediate of O-containing products (methanol and methanal) and traces of methane. Similar results were verified by Koper's group on cobalt protoporphyrin molecular catalyst.[86b] According to the potential-dependent reaction rates and FEs for ethanol, 1-propanol, acetaldehyde, propionaldehyde, methanol, allyl alcohol, and acetone over Cu in a single potential sweep, acetaldehyde is a precursor that forms ethanol and propionaldehyde, whereas propionaldehyde is responsible for the formation of *n*-propanol.[86c, 86d] For the formation of ethylene (Figure 6e),[82] the common intermediate with the formation of methane is observed on the Cu(111) and Cu(100) surfaces. Alternatively, *CO is selectively reduced to ethylene on Cu(100) at relatively low overpotentials presumably via the formation of an adsorbed CO dimer.

To monitor the reaction process during electrocatalysis, *in situ* MS is helpful to qualitatively analyze the catalytic products in real time. Nevertheless, the fragment detection mode of *in situ* MS and the complexity of CO_2RR products make quantitative analysis and the accurate identification of a single product difficult.

5. Other in situ/operando characterization techniques

In addition to the *in situ*/operando techniques mentioned above, other techniques can be applied to detect the dynamic evolution of CO_2RR in real time. For example, *in situ* TEM is powerful to extract structural features of electrocatalysts on nanoscale, including size, shape, surface configuration, and crystalline texture, and even down to atomic scale.[87] The operando morphological transformation of Bi-MOF into single Bi atoms on N-doped carbon networks has been examined by *in situ* TEM.[88] However, the operating condition and the sample preparation for *in situ* TEM experiments are relatively stringent, especially for high-resolution modes. Future advances may facilitate the observation of structural transition and substance migration.

In situ scanning probe microscopy (SPM) is another useful technique to image surface configuration and reveal sub-nanometer features by replacing electrons or light with a physical probe with a sharp tip. The initial form of SPM, scanning tunneling microscopy (STM), is first proposed to image the atomic flat surface,[89] which relies on the quantum tunneling effect of the tiny gap between the sharp probe and flat surface. A recent study aimed to reveal the reconstruction of polycrystalline Cu under working conditions for CO_2RR[90] to correlate the surface structure with the electrocatalytic properties. As another structure-sensitive instrument, atomic force microscopy (AFM) can monitor the surface profile via the tip–sample interaction in Van der Waals forces. Therefore, the requirement of conductive or semiconductive surfaces for STM can be avoided.[87] The observation of morphological changes of Cu cubes via operando electrochemical AFM verified the gradually smoothening corner/edge and decreasing size under electrocatalytic conditions.[91] Advances in operando STM and AFM would further help capture the dynamic information for CO_2RR.

In situ electron spin resonance (ESR) spectroscopy can detect the transitions of unpaired electrons under an applied magnetic field.[92] According to the Pauli exclusion principle, only the species with unpaired electrons exhibit magnetic resonance effects. With the high accuracy of detectable concentration (about 10^{-12} mol), *in situ* ESR spectroscopy has been

used to monitor the radicals produced on the catalyst surface during electrocatalytic reactions. The time-evolution ESR spectra confirmed that both organic ligands of Zr-MOFs and inorganic building unit act as the active sites according to electron paramagnetic resonance signal,[93] thereby providing valuable information to reveal the reaction pathway and mechanism.

6. Conclusions and perspectives

Remarkable efforts have been made to design highly active and/or selective electrocatalysts for CO_2RR. More reaction intermediates, working conditions, and catalytic products have been revealed in real time with the help of *in situ* and operando characterization techniques. These discoveries are helpful to explore the catalytic mechanism of CO_2RR and design efficient catalytic systems. With the induction of possible reaction pathways for CO_2RR toward various C_1 and C_2 products, the working principles, basic configuration, and related research progress of *in situ* characterization techniques, including IR spectroscopy, Raman spectroscopy, XAS, XPS, and MS, were summarized. In brief, recent years witnessed great achievements in the field of *in situ*/operando characterization techniques for CO_2RR. Nonetheless, its ability to identify the specific active sites of an electrocatalytst and the underlying catalytic mechanism due to the complexed reaction with multiple electron transfer remain to be elucidated. Therefore, the implementation of *in situ*/operando techniques in the CO_2RR is still full of challenges and opportunities for future development:

(1) *Combination of in situ/operando techniques to gain deep insights into reaction intermediates.* For the complex CO_2RR, a single *in situ*/operando characterization technique is usually not sufficient for elucidating and resolving the reaction intermediates and pathways involved in the electrocatalytic mechanism. The combination of *in situ* ATR–SEIRAS, isotopic labeling, and MS techniques revealed that the majority of $CO_{2(aq)}$ in the electrolyte originates from equilibrium with bicarbonate rather than the diffusion of $CO_{2(g)}$.[29]. Additionally, a positive correlation between the production of C_{2+} products and the amount of

Cu^+ species has been proposed based on operando XANES and quasi *in situ* XPS measurements.[74b]

(2) *Improving signal intensities of spectroscopy techniques to capture reaction intermediates.* Spectroscopy techniques are highly useful to examine the reaction intermediates without changing the surface status of electrocatalyst and reaction process. Notably, such techniques including FTIR and Raman spectroscopy can be enhanced via surface-enhanced strategies. However, the optimization of such *in situ* spectroscopy techniques is necessary to improve the signal-to-noise ratio by eliminating the negative effect from water molecules and other interferences.

(3) *Ameliorating the rigorous test conditions of some in situ/operando techniques*. The operation of X-ray-based analytical techniques, such as *in situ* XAS and XPS, requires relatively harsh conditions including UHV chamber and high-energy synchrotron. The incorporation of such advanced techniques with the electrocatalytic reactions under ambient conditions is highly dependent on the rational design of *in situ* testing cells to gain deep insight into the electrocatalytic mechanisms associated with CO_2RR.

(4) *Combination of theoretical calculations with in situ experimental analysis.* Some key intermediates are not directly observed due to the multiple step reduction process. The combination of computational calculation and *in situ* experimental analysis can provide a plausible mechanism for carbon dioxide reduction. In particular, machine learning can predict the dynamic evolutions of CO_2RR and infer the reaction mechanism from theoretical analysis by simulating the reaction process under optimized parameters. The rapid development of computational modeling and artificial intelligence may provide predictive guidance to optimize material structures, compositions, and reaction mechanism.

(5) *Direct observation of active sites and reaction intermediates in real time.* The evolution of active sites and intermediates generated under experimental conditions is highly desirable to identify local reacting species with atomic precision and reveal the catalytic mechanism

during CO_2 reduction. Nevertheless, *in situ* techniques can hardly meet the accuracy requirement, and available techniques, such as *in situ* scanning tunneling microscopy or environmental TEM, usually require very rigorous testing conditions. Consequently, developing or improving new *in situ* technologies with high spatial and time resolutions is of great importance to design catalysts with outstanding performance.

(6) *Design of the ideal electrocatalysts to clarify the reaction mechanisms.* With the help of DFT calculations and operando techniques, the ideal electrocatalysts would be rationally designed to reveal the underlying reaction mechanisms of CO_2RR. The obtained insights as the stepping stone can contribute to the identification of real active sites and boost the subsequent design of advanced electrocatalysts.

In summary, serious efforts have already been made, but more will be needed in the years to come to further develop *in situ* and operando characterization techniques that are compatible under CO_2RR conditions.

Acknowledgements

This work was financially supported by the Natural Scientific Foundation (ZR2020JQ09) and Taishan Scholars Program (No. tsqn20161004) of Shandong Province, Project for Scientific Research Innovation Team of Young Scholar in Colleges, Universities of Shandong Province (2019KJC025), and the Fundamental Research Funds of Shandong University (ZY202006).

Received: ((will be filled in by the editorial staff))
Revised: ((will be filled in by the editorial staff))
Published online: ((will be filled in by the editorial staff))

References

[1] a) S. Chu, A. Majumdar, *Nature* **2012**, *488*, 294; b) A. S. Arico, P. Bruce, B. Scrosati, J. M. Tarascon, W. Van Schalkwijk, *Nat. Mater.* **2005**, *4*, 366; c) X. Xiaoding, J. Moulijn, *Energy Fuel.* **1996**, *10*, 305; d) Y. Cheng, S. Yang, S. P. Jiang, S. Wang, *Small Methods* **2019**, *3*, 1800440.

[2] a) J. Tollefson, *Nature* **2009**, *462*, 966; b) Y. Yang, Y. Yang, Y. Liu, S. Zhao, Z. Tang, *Small Sci*. **2021**, 2100015; c) P. Deng, F. Yang, Z. Wang, S. Chen, Y. Zhou, S. Zaman, B. Y. Xia, *Angew. Chem. Int. Ed.* **2020**, *59*, 10807.

[3] a) N. Zhang, R. Long, C. Gao, Y. Xiong, *Sci. China Mater.* **2018**, *61*, 771; b) Y. Quan, J. Zhu, G. Zheng, *Small Sci*. **2021**, 2100043; c) Y. Zhou, Z. Wang, L. Huang, S. Zaman, K. Lei, T. Yue, Z. a. Li, B. You, B. Y. Xia, *Adv. Energy Mater.* **2021**, *11*, 2003159.

[4] a) Y. Hori, H. Wakebe, T. Tsukamoto, O. Koga, *Electrochim. Acta* **1994**, *39*, 1833; b) J. Yang, W. Li, D. Wang, Y. Li, *Small Struct.* **2021**, *2*, 2000051; c) S. Chen, Y. Su, P. Deng, R. Qi, J. Zhu, J. Chen, Z. Wang, L. Zhou, X. Guo, B. Y. Xia, *ACS Catal.* **2020**, *10*, 4640.

[5] a) A. U. Pawar, C. W. Kim, M. T. Nguyen Le, Y. S. Kang, *ACS Sustain. Chem. Eng.* **2019**, *7*, 7431; b) Y. Cheng, X. Wu, J. P. Veder, L. Thomsen, S. P. Jiang, S. Wang, *Energy Environ. Mater.* **2019**, *2*, 5; c) Y. Cheng, S. Zhao, B. Johannessen, J. P. Veder, M. Saunders, M. R. Rowles, M. Cheng, C. Liu, M. F. Chisholm, R. De Marco, H. M. Cheng, S. Z. Yang, S. P. Jiang, *Adv. Mater.* **2018**, *30*, 1706287.

[6] a) K. J. P. Schouten, Y. Kwon, C. J. M. van der Ham, Z. Qin, M. T. M. Koper, *Chem. Sci.* **2011**, *2*, 1902; b) R. X. Yang, Y. R. Wang, G. K. Gao, L. Chen, Y. Chen, S. L. Li, Y. Q. Lan, *Small Struct.* **2021**, *2*, 2100012; c) Z. Wang, Y. Zhou, C. Xia, W. Guo, B. You, B. Y. Xia, *Angew. Chem. Int. Ed.* **2021**, DOI.org/10.1002/anie.202107523.

[7] a) C. Kirk, L. D. Chen, S. Siahrostami, M. Karamad, M. Bajdich, J. Voss, J. K. Nørskov, K. Chan, *ACS Central Sci.* **2017**, *3*, 1286; b) B. Pan, G. Yuan, X. Zhao, N. Han, Y. Huang, K. Feng, C. Cheng, J. Zhong, L. Zhang, Y. Wang, Y. Li, *Small Sci*. **2021**, 2100029.

[8] a) G. Zhang, Y. Jia, C. Zhang, X. Xiong, K. Sun, R. Chen, W. Chen, Y. Kuang, L. Zheng, H. Tang, W. Liu, J. Liu, X. Sun, W. F. Lin, H. Dai, *Energy Environ. Sci.* **2019**, *12*, 1317; b) J. Jiao, R. Lin, S. Liu, W. C. Cheong, C. Zhang, Z. Chen, Y. Pan, J. Tang, K. Wu, S. F. Hung, H. M. Chen, L. Zheng, Q. Lu, X. Yang, B. Xu, H. Xiao, J. Li, D. Wang, Q. Peng, C. Chen, Y. Li, *Nat. Chem.* **2019**, *11*, 222; c) Y. Cheng, J. P. Veder, L. Thomsen, S. Zhao, M. Saunders, R.

Demichelis, C. Liu, R. De Marco, S. P. Jiang, *J. Mater. Chem. A* **2018**, *6*, 1370; d) Y. Cheng, S. Zhao, H. Li, S. He, J. P. Veder, B. Johannessen, J. Xiao, S. Lu, J. Pan, M. F. Chisholm, S. Z. Yang, C. Liu, J. G. Chen, S. P. Jiang, *Appl. Cata. B-Environ.* **2019**, *243*, 294.

[9] A. M. Tripathi, W. N. Su, B. J. Hwang, *Chem. Soc. Rev.* **2018**, *47*, 736.

[10] H. Wang, Y. W. Zhou, W. B. Cai, *Curr. Opin. Electroche.* **2017**, *1*, 73.

[11] A. Wuttig, M. Yaguchi, K. Motobayashi, M. Osawa, Y. Surendranath, *P. Natl. Acad. Sci. USA* **2016**, *113*, E4585.

[12] N. J. Firet, W. A. Smith, *ACS Catal.* **2017**, *7*, 606.

[13] C. M. Gunathunge, V. J. Ovalle, Y. Li, M. J. Janik, M. M. Waegele, *ACS Catal.* **2018**, *8*, 7507.

[14] E. Perez Gallent, M. C. Figueiredo, F. Calle Vallejo, M. T. M. Koper, *Angew. Chem. Int. Ed.* **2017**, *56*, 3621.

[15] S. Zhu, B. Jiang, W. B. Cai, M. Shao, *J. Am. Chem. Soc.* **2017**, *139*, 15664.

[16] a) D. Gao, H. Zhou, F. Cai, D. Wang, Y. Hu, B. Jiang, W. B. Cai, X. Chen, R. Si, F. Yang, S. Miao, J. Wang, G. Wang, X. Bao, *Nano Res.* **2017**, *10*, 2181; b) K. Jiang, H. Wang, W. B. Cai, H. Wang, *ACS Nano* **2017**, *11*, 6451; c) Y. Katayama, L. Giordano, R. R. Rao, J. Hwang, H. Muroyama, T. Matsui, K. Eguchi, Y. Shao Horn, *J. Phys. Chem. C* **2018**, *122*, 12341.

[17] M. Dunwell, Y. Yan, B. Xu, *ACS Catal.* **2017**, *7*, 5410.

[18] A. D. Handoko, F. Wei, Jenndy, B. S. Yeo, Z. W. Seh, *Nat. Catal.* **2018**, *1*, 922.

[19] M. F. Baruch, J. E. Pander, J. L. White, A. B. Bocarsly, *ACS Catal.* **2015**, *5*, 3148.

[20] a) Z. M. Detweiler, J. L. White, S. L. Bernasek, A. B. Bocarsly, *Langmuir* **2014**, *30*, 7593; b) J. E. Pander, M. F. Baruch, A. B. Bocarsly, *ACS Catal.* **2016**, *6*, 7824.

[21] H. L. Chang, M. W. Kanan, *ACS Catal.* **2015**, *5*, 465.

[22] W. Deng, L. Zhang, L. Li, S. Chen, C. Hu, Z. J. Zhao, T. Wang, J. Gong, *J. Am. Chem. Soc.* **2019**, *141*, 2911.

[23] P. Yang, Z. J. Zhao, X. Chang, R. Mu, S. Zha, G. Zhang, J. Gong, *Angew. Chem. Int. Ed.* **2018**, *57*, 7724.

[24] a) A. Wuttig, C. Liu, Q. Peng, M. Yaguchi, C. H. Hendon, K. Motobayashi, S. Ye, M. Osawa, Y. Surendranath, *ACS Central Sci.* **2016**, *2*, 522; b) J. Heyes, M. Dunwell, B. Xu, *J. Phys. Chem. C* **2016**, *120*, 17334.

[25] a) K. Ogura, R. Oohara, Y. Kudo, *J. Electrochem. Soc.* **2005**, *152*, D213; b) Y. Katayama, F. Nattino, L. Giordano, J. Hwang, R. R. Rao, O. Andreussi, N. Marzari, Y. Shao Horn, *J. Phys. Chem. C* **2019**, *123*, 5951.

[26] a) C. W. Li, J. Ciston, M. W. Kanan, *Nature* **2014**, *508*, 504; b) M. M. Sartin, Z. Yu, W. Chen, F. He, Z. Sun, Y. X. Chen, W. Huang, *J. Phys. Chem. C* **2018**, *122*, 26489; c) S. Lee, J. Lee, *ChemElectroChem* **2018**, *5*, 558; d) A. S. Malkani, M. Dunwell, B. Xuo, *ACS Catal.* **2019**, *9*, 474.

[27] T. Cheng, H. Xiao, W. A. Goddard, *J. Am. Chem. Soc.* **2017**, *139*, 11642.

[28] F. Calle Vallejo, M. T. M. Koper, *Angew. Chem. Int. Ed.* **2013**, *52*, 7282.

[29] M. Dunwell, Q. Lu, J. M. Heyes, J. Rosen, J. G. Chen, Y. Yan, F. Jiao, B. Xu, *J. Am. Chem. Soc.* **2017**, *139*, 3774.

[30] A. Murata, Y. Hori, *B. Chem. Soc. JPN.* **1991**, *64*, 123.

[31] a) C. M. Gunathunge, V. J. Ovalle, M. M. Waegele, *Phys. Chem. Chem. Phys.* **2017**, *19*, 30166; b) O. Ayemoba, A. Cuesta, *ACS Appl. Mater. Inter.* **2017**, *9*, 27377; c) E. Perez Gallent, G. Marcandalli, M. C. Figueiredo, F. Calle Vallejo, M. T. M. Koper, *J. Am. Chem. Soc.* **2017**, *139*, 16412; d) J. Resasco, L. D. Chen, E. L. Clark, C. Tsai, C. Hahn, T. F. Jaramillo, K. Chan, A. T. Bell, *J. Am. Chem. Soc. 139*, 11277; e) K. Yang, R. Kas, W. A. Smith, *J. Am. Chem. Soc.* **2019**, *141*, 15891; f) M. Dunwell, X. Yang, Y. Yan, B. Xu, *J. Phys. Chem. C* **2018**, *122*, 24658.

[32] Y. Deng, B. S. Yeo, *ACS Catal.* **2017**, *7*, 7873.

[33] a) M. Fleischmann, P. J. Hendra, A. J. McQuillan, *Chem. Phys. Lett.* **1974**, *26*, 163; b) A. C. Albrecht, *J. Chem. Phys.* **1961**, *34*, 1476; c) A. C. Albrecht, M. C. Hutley, *J. Chem. Phys.* **1971**, *55*, 4438; d) B. Ren, X. Q. Li, C. X. She, D. Y. Wu, Z. Q. Tian, *Electrochim. Acta* **2000**, *46*, 193; e) B. Ren, X. F. Lin, Y. X. Jiang, P. G. Cao, Y. Xie, Q. J. Huang, Z. Q. Tian, *Appl. Spectrosc.* **2003**, *57*, 419; f) W. Akemann, A. Otto, *J. Raman Spectrosc.* **1991**, *22*, 797; g) Z. C. Zeng, S. Hu, S. C. Huang, Y. J. Zhang, W. X. Zhao, J. F. Li, C. Jiang, B. Ren, *Anal. Chem.* **2016**, *88*, 9381.

[34] a) B. S. Yeo, S. L. Klaus, P. N. Ross, R. A. Mathies, A. T. Bell, *ChemPhysChem* **2010**, *11*, 1854; b) D. Ren, Y. Deng, A. D. Handoko, C. S. Chen, S. Malkhandi, B. S. Yeo, *ACS Catal.* **2015**, *5*, 2814; c) D. Ren, B. S. H. Ang, B. S. Yeo, *ACS Catal.* **2016**, *6*, 8239; d) Y. Deng, Y. Huang, D. Ren, A. D. Handoko, Z. W. Seh, P. Hirunsit, B. S. Yeo, *ACS Appl. Mater. Inter.* **2018**, *10*, 28572.

[35] P. Innocenzi, L. Malfatti, *Trac-Trend Anal. Chem.* **2019**, *114*, 233.

[36] N. Heidary, K. H. Ly, N. Kornienko, *Nano Lett.* **2019**, *19*, 4817.

[37] a) Z. Q. Tian, B. Ren, *Annu. Rev. Phys. Chem.* **2004**, *55*, 197; b) B. D. Smith, D. E. Irish, P. Kedzierzawski, J. Augustynski, *J. Electrochem. Soc.* **1997**, *144*, 4288.

[38] A. Dutta, A. Kuzume, M. Rahaman, S. Vesztergom, P. Broekmann, *ACS Catal.* **2015**, *5*, 7498.

[39] I. V. Chernyshova, P. Somasundaran, S. Ponnurangam, *P. Nati. Acad. Sci. USA* **2018**, *115*, E9261.

[40] J. Gao, H. Zhang, X. Guo, J. Luo, S. M. Zakeeruddin, D. Ren, M. Gratzel, *J. Am. Chem. Soc.* **2019**, *141*, 18704.

[41] K. Klingan, T. Kottakkat, Z. P. Jovanov, S. Jiang, C. Pasquini, F. Scholten, P. Kubella, A. Bergmann, B. Roldan Cuenya, C. Roth, H. Dau, *ChemSusChem* **2018**, *11*, 3449.

[42] S. Zhang, P. Kang, T. J. Meyer, *J. Am. Chem. Soc.* **2014**, *136*, 1734.

[43] Y. Ichinohe, T. Wadayama, A. Hatta, *J. Raman Spectrosc.* **1995**, *26*, 335.

[44] a) K. G. Schmitt, A. A. Gewirth, *J. Phys. Chem. C* **2014**, *118*, 17567; b) D. Oehl, Y. U. Kayran, J. R. C. Junqueira, V. Essmann, T. Bobrowski, W. Schuhmann, *Langmuir* **2018**, *34*, 12293.

[45] a) L. Mandal, K. R. Yang, M. R. Motapothula, D. Ren, P. Lobaccaro, A. Patra, M. Sherburne, V. S. Batista, B. S. Yeo, J. W. Ager, J. Martin, T. Venkatesan, *ACS Appl. Mater. Inter.* **2018**, *10*, 8574; b) N. P. Thuy Duong, C. Wang, C. M. Marin, Y. Zhou, E. Stavitski, E. J. Popczun, Y. Yu, W. Xu, B. H. Howard, M. Y. Stuckman, I. Waluyo, P. R. Ohodnicki, Jr., D. R. Kauffman, *J. Mater. Chem. A* **2019**, *7*, 27576.

[46] P. P. Yang, X. L. Zhang, F. Y. Gao, Y. R. Zheng, Z. Z. Niu, X. Yu, R. Liu, Z. Z. Wu, S. Qin, L. P. Chi, Y. Duan, T. Ma, X. S. Zheng, J. F. Zhu, H. J. Wang, M. R. Gao, S. H. Yu, *J. Am. Chem. Soc.* **2020**, *142*, 6400.

[47] H. Yang, Y. Hu, J Chen, M. S. Balogun, P. Fang, S. Zhang, J. Chen, Y. Tong, *Adv. Energy Mater.* **2019**, *9*, 1901396.

[48] a) A. M. Ismail, G. F. Samu, A. Balog, E. Csapo, C. Janaky, *ACS Energy Lett.* **2019**, *4*, 48; b) T. Kottakkat, K. Klingan, S. Jiang, Z. P. Jovanov, V. H. Davies, G. A. M. El Nagar, H. Dau, C. Roth, *ACS Appl. Mater. Inter.* **2019**, *11*, 14734; c) A. Dutta, I. Z. Montiel, R. Erni, K. Kiran, M. Rahaman, J. Drnec, P. Broekmann, *Nano Energy* **2020**, *68*, 104331; d) X. Chen, D. A. Henckel, U. O. Nwabara, Y. Li, A. I. Frenkel, T. T. Fister, P. J. A. Kenis, A. A. Gewirth, *ACS Catal.* **2020**, *10*, 672; e) A. Vasileff, X. Zhi, C. Xu, L. Ge, Y. Jiao, Y. Zheng, S. Z. Qiao, *ACS Catal.* **2019**, *9*, 9411; f) Y. C. Li, Z. Wang, T. Yuan, D. H. Nam, M. Luo, J. Wicks, B. Chen, J. Li, F. Li, F. P. G. de Arguer, Y. Wang, C. T. Dinh, O. Voznyy, D. Sinton, E. H. Sargent, *J. Am. Chem. Soc.* **2019**, *141*, 8584; g) S. Ajmal, Y. Yang, K. Li, M. A. Tahir, Y. Liu, T. Wang, A. U. R. Bacha, Y. Feng, Y. Deng, L. Zhang, *J. Phys. Chem. C* **2019**, *123*, 11555; h) X. Jiang, X. Wang, Z. Liu, Q. Wang, X. Xiao, H. Pan, M. Li, J. Wang, Y. Shao, Z. Peng, Y. Shen, M. Wang, *Appl. Catal. B-Environ.* **2019**, *259*, 118040; i) Y. Yang, S. Ajmal, Y. Feng, K. Li, X. Zheng, L. Zhang, *Chem-Eur. J.* **2020**, *26*, 4080; j) T. T. H. Hoang, S. Verma, S. Ma,

T. T. Fister, J. Timoshenko, A. I. Frenkel, P. J. A. Kenis, A. A. Gewirth, *J. Am. Chem. Soc.* **2018**, *140*, 5791.

[49] Y. Huang, C. W. Ong, B. S. Yeo, *ChemSusChem* **2018**, *11*, 3299.

[50] a) Z. Gong, Y. Yang, *J. Energy Chem.* **2018**, *27*, 1566; b) Michette, Alan, *Contemp. Phys.* **2011**, *52*, 623.

[51] a) J. Yang, S. Muhammad, M. R. Jo, H. Kim, K. Song, D. A. Agyeman, Y. I. Kim, W. S. Yoon, Y. M. Kang, *Chem. Soc. Rev.* **2016**, *45*, 5717; b) C. Bressler, M. Chergui, *Chem. Rev.* **2004**, *104*, 1781.

[52] R. Daiyan, W. H. Saputera, H. Masood, J. Leverett, X. Lu, R. Amal, *Adv. Energy Mater.* **2020**, *10*, 1902106.

[53] H. Mistry, A. S. Varela, C. S. Bonifacio, I. Zegkinoglou, I. Sinev, Y. W. Choi, K. Kisslinger, E. A. Stach, J. C. Yang, P. Strasser, B. Roldan Cuenya, *Nat. Commun.* **2016**, *7*, 12123.

[54] H. S. Jeon, J. Timoshenko, F. Scholten, I. Sinev, A. Herzog, F. T. Haase, B. Roldan Cuenya, *J. Am. Chem. Soc.* **2019**, *141*, 19879.

[55] S. Liu, H. B. Yang, S. F. Hung, J. Ding, W. Cai, L. Liu, J. Gao, X. Li, X. Ren, Z. Kuang, Y. Huang, T. Zhang, B. Liu, *Angew. Chem. Int. Ed.* **2019**, *59*, 798.

[56] a) J. Rosen, G. S. Hutchings, Q. Lu, R. V. Forest, A. Moore, F. Jiao, *ACS Catal.* **2015**, *5*, 4586; b) B. Wang, S. Chu, L. Zheng, X. Li, J. Zhang, F. Zhang, *Small Sci.* **2021**, 2100023.

[57] a) H. Mistry, Y. W. Choi, A. Bagger, F. Scholten, C. S. Bonifacio, I. Sinev, N. J. Divins, I. Zegkinoglou, H. S. Jeon, K. Kisslinger, E. A. Stach, J. C. Yang, J. Rossmeisl, B. Roldan Cuenya, *Angew. Chem. Int. Ed.* **2017**, *56*, 11394; b) K. Ye, Z. Zhou, J. Shao, L. Lin, D. Gao, N. Ta, R. Si, G. Wang, X. Bao, *Angew. Chem. Int. Ed.* **2020**, *59*, 4814; c) X. Zheng, P. De Luna, F. P. G. de Arquer, B. Zhang, N. Becknell, M. B. Ross, Y. Li, M. N. Banis, Y. Li, M. Liu, O. Voznyy, D. Cao Thang, T. Zhuang, P. Stadler, Y. Cui, X. Du, P. Yang, E. H. Sargent, *Joule* **2017**, *1*, 794; d) M. Liu, M. Liu, X. Wang, S. M. Kozlov, Z. Cao, P. De Luna, H. Li, X.

Qiu, K. Liu, J. Hu, C. Jia, P. Wang, H. Zhou, J. He, M. Zhong, X. Lan, Y. Zhou, Z. Wang, J. Li, A. Seifitokaldani, D. Cao Thang, H. Liang, C. Zou, D. Zhang, Y. Yang, T. S. Chan, Y. Han, L. Cavallo, T. K. Sham, B. J. Hwang, E. H. Sargent, *Joule* **2019**, *3*, 1703.

[58] a) W. Sheng, S. Kattel, S. Yao, B. Yan, Z. Liang, C. J. Hawxhurst, Q. Wu, J. G. Chen, *Energy Environ. Sci.* **2017**, *10*, 1180; b) Q. He, J. H. Lee, D. Liu, Y. Liu, Z. Lin, Z. Xie, S. Hwang, S. Kattel, L. Song, J. G. Chen, *Adv. Funct. Mater.* **2020**, *30*, 2000407.

[59] a) P. De Luna, R. Quintero Bermudez, D. Cao Thang, M. B. Ross, O. S. Bushuyev, P. Todorovic, T. Regier, S. O. Kelley, P. Yang, E. H. Sargent, *Nat. Catal.* **2018**, *1*, 103; b) A. Eilert, F. S. Roberts, D. Friebel, A. Nilsson, *J. Phys. Chem. Lett.* **2016**, *7*, 1466; c) N. Dae Hyun, O. S. Bushuyev, J. Li, P. De Luna, A. Seifitokaldani, D. Cao Thang, F. P. G. de Arquer, Y. Wang, Z. Liang, A. H. Proppe, C. S. Tan, P. Todorovic, O. Shekhah, C. M. Gabardo, J. W. Jo, J. Choi, M. J. Choi, S. W. Baek, J. Kim, D. Sinton, S. O. Kelley, M. Eddaoudi, E. H. Sargent, *J. Am. Chem. Soc.* **2018**, *140*, 11378.

[60] H. Xiao, W. A. Goddard, III, T. Cheng, Y. Liu, *P. Natl. Acad. Sci. USA* **2017**, *114*, 6685.

[61] a) C. J. Chang, S. F. Hung, C. S. Hsu, H. C. Chen, S. C. Lin, Y. F. Liao, H. M. Chen, *ACS Central Sci.* **2019**, *5*, 1998; b) N. T. Suen, Z. R. Kong, C. S. Hsu, H. C. Chen, C. W. Tung, Y. R. Lu, C. L. Dong, C. C. Shen, J. C. Chung, H. M. Chen, *ACS Catal.* **2019**, *9*, 5217; c) J. J. Velasco Velez, T. Jones, D. Gao, E. Carbonio, R. Arrigo, C. J. Hsu, Y. C. Huang, C. L. Dong, J. M. Chen, J. F. Lee, P. Strasser, B. Roldan Cuenya, R. Schloegl, A. Knop Gericke, C. H. Chuang, *ACS Sustain. Chem. Eng.* **2019**, *7*, 1485; d) T. C. Chou, C. C. Chang, H. L. Yu, W. Y. Yu, C. L. Dong, J. J. Velasco Velez, C. H. Chuang, L. C. Chen, J. F. Lee, J. M. Chen, H. L. Wu, *J. Am. Chem. Soc.* **2020**, *142*, 2857.

[62] J. Timoshenko, H. S. Jeon, I. Sinev, F. T. Haase, A. Herzog, B. R. Cuenya, *Chem. Sci.* **2020**, *11*, 3727.

[63] a) L. Fang, S. Seifert, R. E. Winans, T. Li, *Small Methods*, **2021**, *5*, 2001194; b) K. Jiang, S. Siahrostami, T. Zheng, Y. Hu, S. Hwang, E. Stavitski, Y. Peng, J. Dynes, M. Gangisetty, D.

Su, K. Attenkofer, H. Wang, *Energy Environ. Sci.* **2018**, *11*, 893; c) H. B. Yang, S. F. Hung, S. Liu, K. Yuan, S. Miao, L. Zhang, X. Huang, H. Y. Wang, W. Cai, R. Chen, J. Gao, X. Yang, W. Chen, Y. Huang, H. M. Chen, C. M. Li, T. Zhang, B. Liu, *Nat. Energy* **2018**, *3*, 140; d) Q. Wang, C. Cai, M. Dai, J. Fu, X. Zhang, H. Li, H. Zhang, K. Chen, Y. Lin, H. Li, J. Hu, M. Miyauchi, M. Liu, *Small Sci.* **2021**, *1*, 2000028.

[64] a) S. Lin, C. S. Diercks, Y. B. Zhang, N. Kornienko, E. M. Nichols, Y. Zhao, A. R. Paris, D. Kim, P. Yang, O. M. Yaghi, C. J. Chang, *Science* **2015**, *349*, 1208; b) B. Zhang, J. Zhang, J. Shi, D. Tan, L. Liu, F. Zhang, C. Lu, Z. Su, X. Tan, X. Cheng, B. Han, L. Zheng, J. Zhang, *Nat. Commun.* **2019**, *10*, 1.

[65] a) Y. Wu, J. Jiang, Z. Weng, M. Wang, D. L. J. Broere, Y. Zhong, G. W. Brudvig, Z. Feng, H. Wang, *ACS Central Sci.* **2017**, *3*, 847; b) C. S. Diercks, S. Lin, N. Komienko, E. A. Kapustin, E. M. Nichols, C. Zhu, Y. Zhao, C. J. Chang, O. M. Yaghi, *J. Am. Chem. Soc.* **2018**, *140*, 1116; c) D. Karapinar, A. Zitolo, T. N. Huan, S. Zanna, D. Taverna, L. H. Galvao Tizei, D. Giaume, P. Marcus, V. Mougel, M. Fontecave, *ChemSusChem* **2020**, *13*, 173; d) Z. Weng, Y. Wu, M. Wang, J. Jiang, K. Yang, S. Huo, X. F. Wang, Q. Ma, G. W. Brudvig, V. S. Batista, Y. Liang, Z. Feng, H. Wang, *Nat. Commun.* **2018**, *9*, 415; e) C. Xu, X. Zhi, A. Vasileff, D. Wang, B. Jin, Y. Jiao, Y. Zheng, S. Z. Qiao, *Small Struct.* **2021**, *2*, 2000058.

[66] a) C. Papp, H. P. Steinrueck, *Surf. Sci. Rep.* **2013**, *68*, 446; b) T. Masuda, H. Yoshikawa, H. Noguchi, T. Kawasaki, M. Kobata, K. Kobayashi, K. Uosaki, *Appl. Phys. Lett.* **2013**, *103*, 111605.

[67] Y. S. Liu, S. Jeong, J. L. White, X. Feng, E. S. Cho, V. Stavila, M. D. Allendorf, J. J. Urban, J. Guo, *ChemPhysChem* **2019**, *20*, 1261.

[68] K. Roy, L. Artiglia, J. A. van Bokhoven, *ChemCatChem* **2018**, *10*, 666.

[69] a) M. J. Williamson, R. M. Tromp, P. M. Vereecken, R. Hull, F. M. Ross, *Nat. Mater.* **2003**, *2*, 532; b) J. M. Grogan, H. H. Bau, *J. Microelectromech. S.* **2010**, *19*, 885.

[70] Y. W. Choi, F. Scholten, I. Sinev, B. Roldan Cuenya, *J. Am. Chem. Soc.* **2019**, *141*, 5261.

[71] F. Scholten, I. Sinev, M. Bernal, B. Roldan Cuenya, *ACS Catal.* **2019**, *9*, 5496.

[72] A. Eilert, F. Cavalca, F. S. Roberts, J. Osterwalder, C. Liu, M. Favaro, E. J. Crumlin, H. Ogasawara, D. Friebel, L. G. M. Pettersson, A. Nilsson, *J. Phys.l Chem. Lett.* **2017**, *8*, 285.

[73] a) A. A. Permyakova, J. Herranz, M. El Kazzi, J. S. Diercks, M. Povia, L. R. Mangani, M. Horisberger, A. Patru, T. J. Schmidt, *ChemPhysChem* **2019**, *20*, 3120; b) X. Chang, T. Wang, Z. J. Zhao, P. Yang, J. Greeley, R. Mu, G. Zhang, Z. Gong, Z. Luo, J. Chen, Y. Cui, G. A. Ozin, J. Gong, *Angew. Chem. Int. Ed.* **2018**, *57*, 15415.

[74] a) D. Gao, I. Zegkinoglou, N. J. Divins, F. Scholten, I. Sinev, P. Grosse, B. Roldan Cuenya, *ACS Nano* **2017**, *11*, 4825; b) D. Gao, I. Sinev, F. Scholten, R. M. Aran Ais, N. J. Divins, K. Kvashnina, J. Timoshenko, B. Roldan Cuenya, *Angew. Chem. Int. Ed.* **2019**, *58*, 17047.

[75] M. Bernal, A. Bagger, F. Scholten, I. Sinev, A. Bergmann, M. Ahmadi, J. Rossmeisl, B. Roldan Cuenya, *Nano Energy* **2018**, *53*, 27.

[76] a) B. Bozzini, M. Amati, C. Mele, A. Knop Gericke, E. Vesselli, *J. Electroanal. Chem.* **2017**, *799*, 17; b) Y. Yu, B. Mao, A. Geller, R. Chang, K. Gaskell, Z. Liu, B. W. Eichhorn, *Phys. Chem. Chem. Phys.* **2014**, *16*, 11633.

[77] a) A. H. Wonders, T. H. M. Housmans, V. Rosca, M. T. M. Koper, *J. Appl. Electrochem.* **2006**, *36*, 1215; b) J. P. Grote, A. R. Zeradjanin, S. Cherevko, K. J. J. Mayrhofer, *Rev. Sci. Instrum.* **2014**, *85*, 104101.

[78] M. Soriaga, J. Baricuatro, A. Javier, Y. G. Kim, K. Cummins, C. Tsang, J. Hemminger, N. Bui, J. Stickney, *Electrocatalysis*, **2018**, *9*, 526.

[79] H. Baltruschat, *J. Am. Soc. Mass Spectr.* **2004**, *15*, 1693.

[80] E. L. Clark, M. R. Singh, Y. Kwon, A. T. Bell, *Anal. Chem.* **2015**, *87*, 8013.

[81] J.-P. Grote, A. R. Zeradjanin, S. Cherevko, A. Savan, B. Breitbach, A. Ludwig, K. J. J. Mayrhofer, *J. Catal.* **2016**, *343*, 248.

[82] K. J. P. Schouten, Z. Qin, E. P. Gallent, M. T. M. Koper, *J. Am. Chem. Soc.* **2012**, *134*, 9864.

[83] a) P. Abbasi, M. Asadi, C. Liu, S. Sharifi Asl, B. Sayahpour, A. Behranginia, P. Zapol, R. Shahbazian Yassar, L. A. Curtiss, A. Salehi Khojin, *ACS Nano* **2017**, *11*, 453; b) D. Plana, J. Florez Montano, V. Celorrio, E. Pastor, D. J. Fermin, *Chem. Commun.* **2013**, *49*, 10962; c) W. O. Silva, G. C. Silva, R. F. Webster, T. M. Benedetti, R. D. Tilley, E. A. Ticianelli, *ChemElectroChem* **2019**, *6*, 4626; d) A. Javier, J. H. Baricuatro, Y. G. Kim, M. P. Soriaga, *Electrocatalysis* **2015**, *6*, 493; e) N. Todoroki, H. Tei, H. Tsurumaki, T. Miyakawa, T. Inoue, T. Wadayama, *ACS Catal.* **2019**, *9*, 1383.

[84] P. Khanipour, M. Loeffler, A. M. Reichert, F. T. Haase, K. J. J. Mayrhofer, I. Katsounaros, *Angew. Chem. Int. Ed.* **2019**, *58*, 7273.

[85] R. Kas, R. Kortlever, A. Milbrat, M. T. M. Koper, G. Mul, J. Baltrusaitis, *Phys. Chem. Chem. Phys.* **2014**, *16*, 12194.

[86] a) G. M. Brisard, A. P. M. Camargo, F. C. Nart, T. Iwasita, *Electrochem. Commun.* **2001**, *3*, 603; b) J. Shen, R. Kortlever, R. Kas, Y. Y. Birdja, O. Diaz Morales, Y. Kwon, I. Ledezma Yanez, K. J. P. Schouten, G. Mul, M. T. M. Koper, *Nat. Commun.* **2015**, *6*, 1; c) E. L. Clark, A. T. Bell, *J. Am. Chem. Soc.* **2018**, *140*, 7012; d) M. Loeffler, P. Khanipour, N. Kulyk, K. J. J. Mayrhofer, I. Katsounaros, *ACS Catal.* **2020**, *10*, 6735; e) A. Javier, B. Chmielowiec, J. Sanabria Chinchilla, Y. G. Kim, J. H. Baricuatro, M. P. Soriaga, *Electrocatalysis* **2015**, *6*, 127.

[87] A. D. Handoko, F. Wei, Jenndy, B. S. Yeo, Z. W. Seh, *Nat. Catal.* **2018**, *1*, 922.

[88] E. Zhang, T. Wang, K. Yu, J. Liu, W. Chen, A. Li, H. Rong, R. Lin, S. Ji, X. Zheng, Y. Wang, L. Zheng, C. Chen, D. Wang, J. Zhang, Y. Li, *J. Am. Chem. Soc.* **2019**, *141*, 16569.

[89] S. Kano, T. Tada, Y. Majima, *Chem. Soc. Rev.* **2015**, *44*, 970.

[90] T. H. Phan, K. Banjac, F. P. Cometto, F. Dattila, R. García-Muelas, S. J. Raaijman, C. Ye, M. T. M. Koper, N. López, M. Lingenfelder, *Nano Lett.* **2021**, *21*, 2059.

[91] P. Grosse, D. Gao, F. Scholten, I. Sinev, H. Mistry, B. Roldan. Cuenya, *Angew. Chem. Int. Ed.* **2018**, *57*, 6192.

[92] X. Li, S. Wang, L. Li, Y. Sun, Y. Xie, *J. Am. Chem. Soc.* **2020**, *142*, 9567.

[93] D. Chen, H. Xing, C. Wang, Z. Su, *J. Mater. Chem. A* **2016**, *4*, 2657.

Xueying Cao received her bachelor's degree in 2016 and master's degree in 2019 from the Department of Materials Science and Engineering, Qingdao University, China. Currently, she is a doctoral student in Prof. Jintao Zhang's group. Her current research is focused on non-noble metal-based materials for electrochemical carbon dioxide reduction.

Jintao Zhang obtained his Ph.D. from the Department of Chemical and Biomolecular Engineering at the University of Singapore in 2012. He was a postdoctoral fellow at Nanyang Technological University (Singapore) and Case Western Reserve University (USA). In fall 2015, he joined the School of Chemistry and Chemical Engineering, Shandong University as a full professor. His research interests include the rational design and synthesis of advanced materials for electrocatalysis, electrochemical energy storage, and conversion (e.g., Zn–air battery, halogen-based batteries, fuel cells, and supercapacitors).

With an introduction on reaction pathways of CO_2RR for generating various products, recent advances in the development and applications of *in situ* and operando characterization techniques to reveal the electrocatalytic mechanisms are reviewed, followed by suggestions and future directions of in situ/operando analysis.

*Xueying Cao, Dongxing Tan, Bari Wulan, K.S. Hui, K.N. Hui, Jintao Zhang**

***In situ* characterization for boosting electrocatalytic carbon dioxide reduction**